Physics – Uspekhi **69** (1) 25 – 41 (2026)

REVIEWS OF TOPICAL PROBLEMS

PACS numbers: 41.60.Cr, 61.05.cj, 61.10.Ht, 71.45.Lr, 74.20.Mn, 74.25.Dw, **74.70. – b**, 74.72.Cj, **78.47. + p**

Real-space pairing and formation of Fermi–Bose mixture in $BaBiO_3$-based family of superconducting oxides

A.P. Menushenkov, M.Yu. Kagan

DOI: https://doi.org/10.3367/UFNe.2025.09.040028

Contents

Abstract. Recently, using X-ray free-electron laser radiation, the first direct experimental evidence of the existence of a real-space paired state of charge carriers was obtained in the parent compound $BaBiO_3$ of the bismuthate family of high-temperature superconductors (HTSCs), whose perovskite-like structure is similar to that of cuprate HTSCs. This confirmed the fundamental premises of our previously formulated model of a spatially separated Fermi–Bose mixture, implying a new, original mechanism for high-temperature superconductivity in bismuthates. In this review, we discuss the progress achieved with this model based on results obtained with an X-ray free-electron laser and go through details of the complete phase diagram of the superconducting and normal states in $Ba_{1-x}K_xBiO_3$ bismuth oxides at various potassium doping concentrations. We also discuss new, unique quantum states of matter in the form of a bosonic insulator (semiconductor) with initially paired charge carriers and two energy gaps, and a bosonic metal shunted by a fermionic component. We also provide experimental evidence that local pairing of electrons and holes is responsible for the set of the main anomalous properties of the bismuthate family. Given the numerous similarities in the behavioral patterns of various families of perovskite superconductors, we believe that our work will provide new impetus to understanding the nature of high-temperature superconductivity in bismuth oxides and other families, including cuprate HTSCs.

Keywords: high-temperature superconductivity, perovskite structure, Fermi–Bose mixture, real-space pairing

A.P. Menushenkov [(1, *)], **M.Yu. Kagan** [(2, 3, †)]
[(1)] National Research Nuclear University MEPhI, Kashirskoe shosse 31, 115409 Moscow, Russian Federation
[(2)] HSE University, ul. Myasnitskaya 20, 101000 Moscow, Russian Federation
[(3)] Kapitza Institute for Physical Problems, Russian Academy of Sciences, ul. Kosygina 2, 119334 Moscow, Russian Federation
E-mail: [(*)] apmenushenkov@mephi.ru, [(†)] kagan@kapitza.ras.ru

Received 8 April 2025, revised 5 September 2025
Uspekhi Fizicheskikh Nauk **196** (1) 29 – 48 (2026)
Translated by S. Alekseev

1. Introduction

The anomalous nature of superconductivity and the unusual characteristics of the normal state in both the metallic and insulating phases in bismuth oxides $Ba_{1-x}K_xBiO_3$ have long attracted the attention of theorists and experimentalists dealing with various high-temperature superconductivity mechanisms and materials, both in this country and abroad.

Already in the early theoretical works of Rice and Sneddon [1] and Varma [2], the superconductivity mechanism was based on Anderson's classic work on negative U-centers in amorphous glasses and $Pb_{1-x}Tl_xTe$-type semiconducting superconductors [3] (see also the experimental work of Chernik at the Leningrad Physico-Technical Institute [4]).

In the work of Rice and Sneddon, the negative sign for the Hubbard potential at a single site emerged due to the interaction of electrons with optical phonons and the formation of local pairs (bipolarons) at bismuth sites. In this approach, the attraction effect for the Hubbard potential naturally arises in the second order of electron–phonon coupling, starting with the Holstein Hamiltonian [1].

At the same time, in his famous article on variable valence in bismuth oxides [2], Varma adhered to a different concept regarding the local pair formation mechanism. He believed that the underlying ideas must be those of quantum chemistry regarding the absence of valence +4 for bismuth ions and the emergence of a charge density wave state (charge dispropor-

tionation) with numerically equal and spatially alternating sites of bismuth ions with valence +5 and valence +3.

In other words, one can say that many elements, including Bi and Tl, tend towards filled s-shells ($6s^2$ for Bi^{3+} and $6s^0$ for Bi^{5+}) and avoid half-filled shells $6s^1Bi^{4+}$, which, according to Varma's idea, can lead to the emergence of effective (intra-atomic) attraction at the Bi site (more precisely, from our standpoint, at the BiO_6 octahedron, which is the main structural block of these perovskite materials). At the same time, for the interaction between neighboring bismuth sites, according to Varma, Coulomb repulsion can dominate, leading to the formation of a charge density wave with alternating Bi^{3+} and Bi^{5+} sites. We note one more circumstance very important for charge disproportionation, related to the different ionic radii for bismuth and thallium with empty and completely filled s-shells.

Later development of works on valence disproportionation and the significance of the Varma effect for the emergence of superconductivity in various exotic materials, including silver and gold alloys, is considered in detail in review articles and reports by Miyake's group [5] and Khomskii et al. [6].

In this review, we adopt a standpoint close to Varma's ideas, but augment his superconductivity scenario with several very important points, because our model is based on experimental XANES (X-ray Absorption Near Edge Structure) [7, 8] and EXAFS (Extended X-ray Absorption Fine Structure) [9, 10] data with synchrotron radiation, which we were the first in the world to apply to the study of the local properties of superconducting oxides [11]. Namely, as we have already indicated, we work not at the level of individual bismuth sites but at the level of the major structural blocks, the BiO_6 octahedra, which are the most rigidly bound elements of the perovskite lattice and can be regarded as quasimolecular complexes. At the same time, we distance ourselves from the simple ionic model of bismuth valence disproportionation $2Bi^{4+} \rightarrow Bi^{3+} + Bi^{5+}$, which is inconsistent with the absence of splitting of the 4f Bi lines in experiments on photoelectron spectroscopy; instead, we use the $2Bi^{4+} \rightarrow Bi^{3+} + Bi^{3+}\underline{L}^2$ pattern (where $\underline{L}^2$ denotes a pair of holes distributed over the entire oxygen environment of bismuth in the $Bi\underline{L}^2O_6$ complex), which we first proposed in [7, 8] and which entered the literature under the name of the Bi6s–O2p bond disproportionation scheme [12].

In addition, we for the first time put forward the concept of local pairing of electrons and holes on neighboring octahedral complexes, formulated in the form of a new model of Bi6s–O2p_{σ^*}-bond disproportionation, $2Bi\underline{L}^1O_6 \rightarrow Bi\underline{L}^0O_6 + Bi\underline{L}^2O_6$; we experimentally prove the existence of a double-well potential of oxygen ion oscillations at the boundary of different BiO_6 octahedra, arising as a result of two-particle tunneling of local pairs between neighboring octahedra [10]. Moreover, we put forward the idea of a possible dynamical nature of pairing, inherently related to the features of the local electron and crystal structure of bismuth oxides in the form of oscillations of oxygen ions in the double-well potential in accordance with the dynamical exchange $Bi\underline{L}^0O_6 \leftrightarrow Bi\underline{L}^2O_6$ [13].

Next, we introduce the concepts of new quantum states of matter, including the state of a local pair density wave (LPDW), generalizing Varma's idea of a charge density wave, and a bosonic semiconductor (containing local pairs and having a two-particle transport activation nature) for the parent compound $BaBiO_3$ in the absence of potassium doping ($x = 0$).

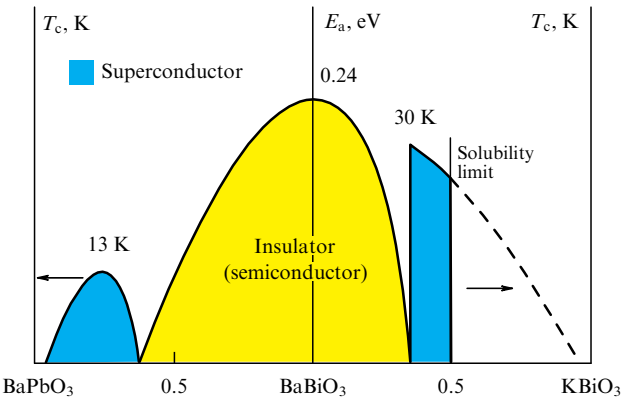

Figure 1. Global phase diagram of family of high-temperature superconducting $BaBiO_3$-based oxides under doping with lead and potassium. Regions of superconducting pairing for both systems with dependence of T_c on doping level of Pb and K, dielectric (semiconductor) state of both systems with activation energy E_a, and phase separation region (for $BaKBiO_3$) are shown. (Diagram is qualitative and vertical scales of insulating and superconducting phases are different.)

We also introduce the concept of a bosonic metal and a Fermi–Bose mixture of bosonic clusters with local electron pairs and fermionic clusters with unpaired hole states to describe various regions of the phase diagram of $Ba_{1-x}K_xBiO_3$, depending on the potassium concentration x. We discuss the nature of the bosonic semiconductor–bosonic metal percolation phase transition (shunted by a fermionic component) and the nature of the emergence of a coherent superconducting state as a result of tunneling of local pairs through a fermionic cluster for critical potassium concentrations $x \geqslant 0.37$.

Finally, we discuss the state of a normal Fermi metal in $KBiO_3$ at the other end of the phase diagram at the potassium concentration $x = 1$, accounting for the existence of a solubility limit of potassium in $BaBiO_3$ $x \approx 0.5$ and the impossibility of synthesizing the $KBiO_3$ compound, and relying on the properties of its actually existing electronic analogue $BaPbO_3$.

We present new experimental data obtained in a unique experiment with tr-XAS (time-resolved X-ray absorption spectroscopy) that we conducted with the European X-ray Free-Electron Laser (EuXFEL) [13, 14], which fully confirmed our interpretation of the phase diagram of the bismuthate family (Fig. 1), the concept of local pairing, and the mechanism of two-particle transport [10], and provided additional evidence in favor of our model of the superconductivity mechanism in bismuth oxides in the form of a spatially separated Fermi–Bose mixture [15–17].

2. Anomalous properties of family of $BaBiO_3$-based high-temperature superconductors

Superconductivity in the family of superconducting oxides with a perovskite structure based on $BaBiO_3$ (bismuthates) in the $BaPb_{1-x}Bi_xO_3$ (BPBO) compound with the critical temperature $T_c \approx 13$ K was discovered already in 1975 [18], 11 years before the discovery of high-temperature superconductivity in cuprates [19]. However, this family was recognized as a high-temperature superconductor (HTSC)

only two years after the discovery by Bednorz and Müller — in 1988, when superconductivity with $T_c \approx 30$ K was discovered in the $Ba_{1-x}K_xBiO_3$ (BKBO) compound [20].

In recent years, the parent compound of the $BaBiO_3$ bismuthate family has attracted a new wave of attention from both theoretical and experimental communities in condensed matter physics (see review [12] and the references therein). Moreover, this family mainly attracts interest because there is still no unified explanation for either the insulating state in the initial $BaBiO_3$ or the superconductivity mechanism in doped bismuthates [12].

After the discovery of superconductivity in $BaPb_{0.25}Bi_{0.75}O_3$ and $Ba_{0.6}K_{0.4}BiO_3$, bismuthates were widely studied using the most modern methods. However, the unusual properties of the $BaBiO_3$ parent compound (which, according to band calculations, should be a metal and have an ideal cubic structure, but is actually an insulator with a monoclinically distorted structure), which were largely described already in the early review by Uchida et al. [21], have not yet been consistently explained.

Among the most important anomalies of this family, the following ones are highlighted in [21]: the presence of two energy gaps, an optical one $E_G \approx 1.96$ eV and a transport (activation) one $E_a \approx 0.24$ eV; anomalously high concentration of charge carriers in the insulating $BaBiO_3$, equal to the concentration of unit cells, which indicates the absence of the impurity conductivity mechanism; an anomalously low density of states at the Fermi level in superconducting oxides $BaPb_{0.75}Bi_{0.25}O_3$ and $Ba_{0.6}K_{0.4}BiO_3$; and an anomalously large breathing mode amplitude in Raman scattering (~ 570 cm^{-1}) under resonant laser excitation through the optical gap. As a result of these observations, it was suggested in [21] that the unusual electronic and structural properties of $BaBiO_3$ can be satisfactorily explained only if all charge carriers are assumed to be a paired state and conductivity to be due to two-particle transport, apparently in a bipolaron description. Thus, the main question raised by the authors of [21] is about the nature of the ground state of the initial compound.

We believe that the answer to this question is key to understanding not only the insulating state in $BaBiO_3$ but also the superconductivity mechanism in doped bismuthates.

Approaches described in the literature explain the insulating ground state of $BaBiO_3$ on the basis of charge disproportionation, conventionally divided into two groups: disproportionation of bismuth valence and disproportionation of bonds of hybridized Bi6s and O2p orbitals. Both approaches give rise to breathing distortions in the perovskite lattice of $BaBiO_3$ [12].

Several different models of Bi valence disproportionation $2Bi^{4+} \rightarrow Bi^{3+} + Bi^{5+}$ have been proposed [1, 2, 22–24]. However, as already mentioned in Section 1, this scenario is not consistent with the results of photoemission spectroscopy, which showed the absence of splitting of Bi 4f core states [25, 26]. Some electron structure calculations using linearized augmented plane waves (LAPWs) [27, 28] and density functional theory (DFT) [29, 30] also indicated the absence of a noticeable charge difference at the two bismuth positions. To conciliate contradictions, Rice's concept of a local commensurate charge density wave (CDW) was proposed [21, 27, 28, 31]. In addition, several models of charge disproportionation with a noninteger bismuth valence $Bi^{4\pm\delta}$ ($0 < \delta < 1$) have been developed [32, 33].

Another approach, based on the $2Bi^{4+} \rightarrow Bi^{3+} + Bi^{3+}\underline{L}^2$ pattern (here, $\underline{L}^2$ denotes two holes distributed over the six oxygen atoms surrounding the Bi ion), was first proposed by us based on the results of studying the effect of oxygen deficiency [34] on XANES spectra [7, 8] and became known in the literature as 'disproportionation of Bi6s–O2p bonds' [12]. This approach does not contradict the results of photoemission spectroscopy, because both bismuth ions are in the same valence state Bi^{3+}, it has been implemented in various models [29, 30, 35, 36], and it is often regarded as preferable [12]. However, these models do not directly account for the existence of a paired state of charge carriers [21] in the initial $BaBiO_3$, assuming that either the breathing lattice distortion [29] or the different local environment of bismuth atoms [30] is responsible for the disproportionation of the Bi6s–O2p bond. Moreover, the cited models do not explain the splitting of Bi 4f lines observed in high-resolution photoelectron spectra [25] in the superconducting phase of $Ba_{1-x}K_xBiO_3$, which, from our standpoint [10], indicates the appearance of two valence states of bismuth upon doping, in contrast to the initial $BaBiO_3$.

As a result of low-temperature EXAFS studies of $BaBiO_3$ [9, 10], we discovered the presence of anomalous lattice oscillations at low temperatures, which we explained by the existence of local pairing of electrons and holes on neighboring octahedral complexes. It has been established that different electron filling of the upper antibonding orbital Bi6s–O2p$_{\sigma^*}$ of neighboring octahedral complexes BiO_6 and the possibility of mutual tunneling of local pairs between complexes give rise to a double-well potential of oxygen ion oscillations.

The concept of local pairing in real space thus emerged, formulated in the form of a new model of Bi6s–O2p$_{\sigma^*}$-bond disproportionation $2Bi\underline{L}^1O_6 \rightarrow Bi\underline{L}^0O_6 + Bi\underline{L}^2O_6$ [10], which explains the set of ground state anomalies of $BaBiO_3$ noted in [21]. In this model, $Bi\underline{L}^2O_6$ represents a small octahedron carrying a pair of holes $\underline{L}^2$, which behaves like a rigid molecule with a vacant upper antibonding orbital Bi6s–O2p$_{\sigma^*}$, and $Bi\underline{L}^0O_6$ is a large soft octahedron carrying an electron pair and exhibiting properties similar to a weakly bound molecule with a completely filled upper antibonding orbital Bi6s–O2p$_{\sigma^*}$. It is local pairing that creates the monoclinic distortion of the cubic lattice of $BaBiO_3$, including breathing and rotational distortions. A local electron pair can then tunnel between neighboring complexes in accordance with the dynamical exchange $Bi\underline{L}^0O_6 \leftrightarrow Bi\underline{L}^2O_6$, causing oscillations of the oxygen atom in the double-well potential. Resonant laser excitation across the optical gap $E_G \approx 1.96$ eV should lead to local pair breaking, and the structure of $BaBiO_3$ in the excited state represents a system of identical $Bi\underline{L}^1O_6$ octahedra with one electron and one hole on the upper antibonding Bi6s–O2p$_{\sigma^*}$ orbital [10] (Fig. 2).

From this standpoint, invoking the concept of Anderson's negative U′ potential [38, 39], the initial $BaBiO_3$ compound can also be regarded as a system with rigidly bound bosons with a real-space lattice [37] (i.e., with only one boson per site [2]). At the same time, it is asserted in a number of studies that the electron and hole pairing mechanism in $BaBiO_3$ has an electronic [2, 38, 39], rather than a phonon (bipolaron) [1, 21, 29, 30, 35, 36, 40, 41], nature.

At the same time, the exact local pair formation mechanism and the relation between the superconductivity mechanism and the local crystal and electron structure in

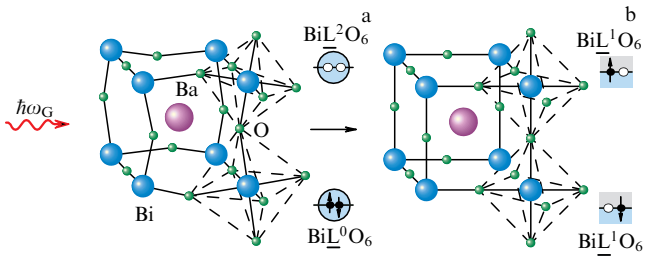

Figure 2. Local crystal and electron structure of $BaBiO_3$ in ground and excited states. (a) Ground state with large $Bi\underline{L}^0O_6$ and small $Bi\underline{L}^2O_6$ octahedra respectively carrying pairs of electrons $\underline{L}^0$ and holes $\underline{L}^2$ on upper antibonding orbital Bi6s–O2p$_{\sigma^*}$. (b) Excited state after resonant laser excitation $\hbar\omega_G$ through optical gap with destroyed pairs and equal octahedra. Circles show paired states, and $\underline{L}^2$, $\underline{L}^0$, and $\underline{L}^1$ respectively denote a local hole pair, a local electron pair, and a single electron (hole) (from [10]).

$Ba_{1-x}K_xBiO_3$ are still being actively discussed. In this review, we substantiate the standpoint that local pairs of electrons and holes form simultaneously [10, 13] in neighboring octahedral complexes BiO_6, which are the main building blocks in superconducting bismuthates, similar to CuO_4 blocks in HTSC cuprates [42–46].

We present our new experimental data confirming that the ground insulating state of the parent compound $BaBiO_3$ can be regarded as a two-particle (bosonic) analogue of a conventional semiconductor with an energy gap $2E_a$ and a bosonic chemical potential μ_0 at the center of this gap. This μ_0 level is common for all octahedra, which determines the absence of splitting of Bi 4f states referenced to μ_0, and indicates the identical valence state of all bismuth ions Bi^{3+} in the initial $BaBiO_3$ [13, 14].

We show that the ground state of the parent compound corresponds to an LPDW (generalizing Varma's early ideas about the emergence of a CDW in bismuth oxides [2]).

Taking the results of the experiment recently conducted at XFEL [14] into account, we also throughly consider the scenario of the formation of a spatially separated Fermi–Bose mixture that we proposed earlier and the nature of superconductivity in bismuth oxides $Ba_{1-x}K_xBiO_3$ at $x \geqslant 0.37$ [15–17]. We emphasize that this model is inextricably linked with the features of the crystal and electron structure of bismuthates, caused by the presence of a double-well potential of oxygen ion oscillations in the BiO_6 octahedra due to local pairing of charge carriers [10]. We also note that, based on the model considered here, we recently proposed a new explanation for the metallic state in barium plumbate $BaPbO_3$ and consistently demonstrated the features of the formation of a spatially separated Fermi–Bose mixture under doping $BaBiO_3$ with lead [13].

We show that superconductivity in bismuth oxides and the formation of the macroscopic wave function of the superconducting state are due to the tunneling of a local electron pair from one bosonic cluster containing local pairs to a neighboring cluster through a normal (free of paired states) fermionic barrier in the double-well structure of the effective ionic potential.

We also note the possibilities of using the basic two-particle physics of the T-matrix approximation for the formation of the lower and upper Hubbard bands [47, 48] to explain experimental data indicating the transformation of the two-particle spectrum of the ground state into a single-particle spectrum of an excited state [14].

3. Features of local electron and crystal structure of $Ba_{1-x}K_xBiO_3$

We emphasize that the three-dimensional cubic structure of bismuthates differs from the quasi-two-dimensional structure of layered HTSC cuprates. As we already mentioned in Section 2, the building blocks in bismuthates are the octahedral complexes BiO_6, while in superconducting metallic CuO_2 layers of HTSC cuprates, the building blocks are the elementary CuO_4 plaquettes.

We note that a similar CuO_6 block, for example, in $La_{2-x}Ba_xCuO_4$, arises only when two additional oxygen ions (so-called apical ions) on two LaO or BaO layers of the charge reservoir adjacent to the conducting CuO_2 layer are taken into account.

We emphasize that the elementary CuO_4 plaquette in the metallic CuO_2 layer plays a crucial role in the superconductivity mechanism in cuprates with a high superconducting transition temperature. Namely on this plaquette are the famous Zhang–Rice singlets formed [44]. It is the Zhang–Rice construction with a copper spin surrounded by four oxygen spins that determines the transition from the two-band superconductivity scenario (proposed by Emery et al. [49] and supported by Unger and Fulde [42]) to Anderson's effective single-band theory [43], described by the generalized $t-J$ model and its d-wave superconductivity [45, 46].

Returning to bismuthates, we note that octahedral BiO_6 complexes are the most rigidly bound structural elements in $BaBiO_3$-based oxides, which corresponds to the strong covalent nature of the Bi6s–O2p chemical bond.

Crystallographic data [22, 23] suggest that the crystal structure of the $BaBiO_3$ parent compound corresponds to an ordered alternation of expanded and compressed BiO_6 octahedra.

As noted above, the results in [10] show that the larger soft octahedron corresponds to a $Bi\underline{L}^0O_6$ complex with the completely filled antibonding orbital Bi6s–O2p$_{\sigma^*}$, and the smaller rigid octahedron corresponds to a $Bi\underline{L}^2O_6$ complex with a free level on the upper antibonding orbital Bi6s–O2p$_{\sigma^*}$ (Fig. 3).

According to [10] and Figs 2 and 3, the larger soft $Bi\underline{L}^0O_6$ complex contains 20 electrons, which corresponds to the formation of a local $\underline{L}^0$ electron pair on the upper antibonding orbital Bi6s–O2p$_{\sigma^*}$, and the smaller rigid complex $Bi\underline{L}^2O_6$ contains 18 electrons, and a local hole pair $\underline{L}^2$ forms on the antibonding orbital Bi6s–O2p$_{\sigma^*}$ in it.

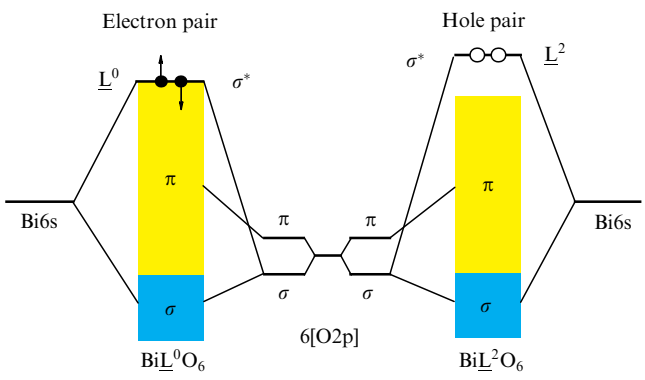

Figure 3. Diagram of formation of local electron structure of neighboring octahedral complexes $Bi\underline{L}^0O_6$ and $Bi\underline{L}^2O_6$ in $BaBiO_3$ (from [10]).

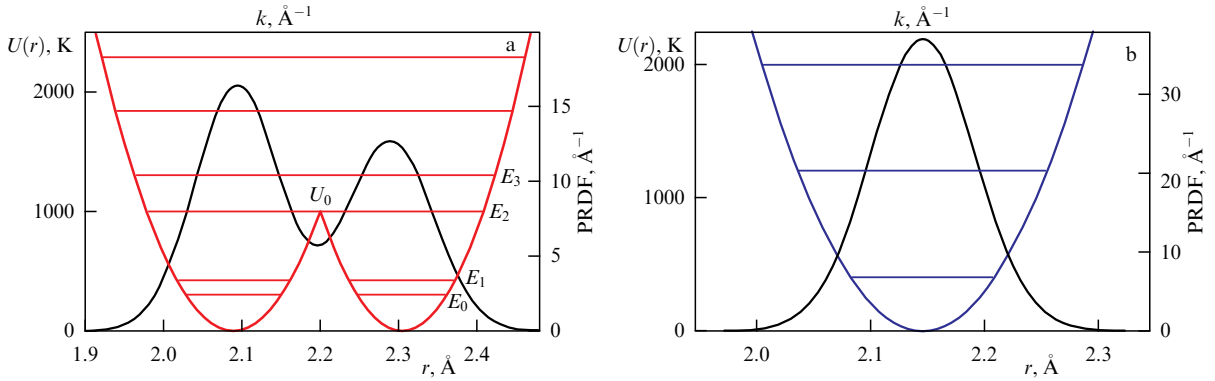

Figure 4. Pair radial distribution functions of atoms and potentials of oxygen ion oscillations: (a) double-well in $BaBiO_3$ and (b) harmonic in $BaPbO_3$ at temperature of 7 K (from [10]).

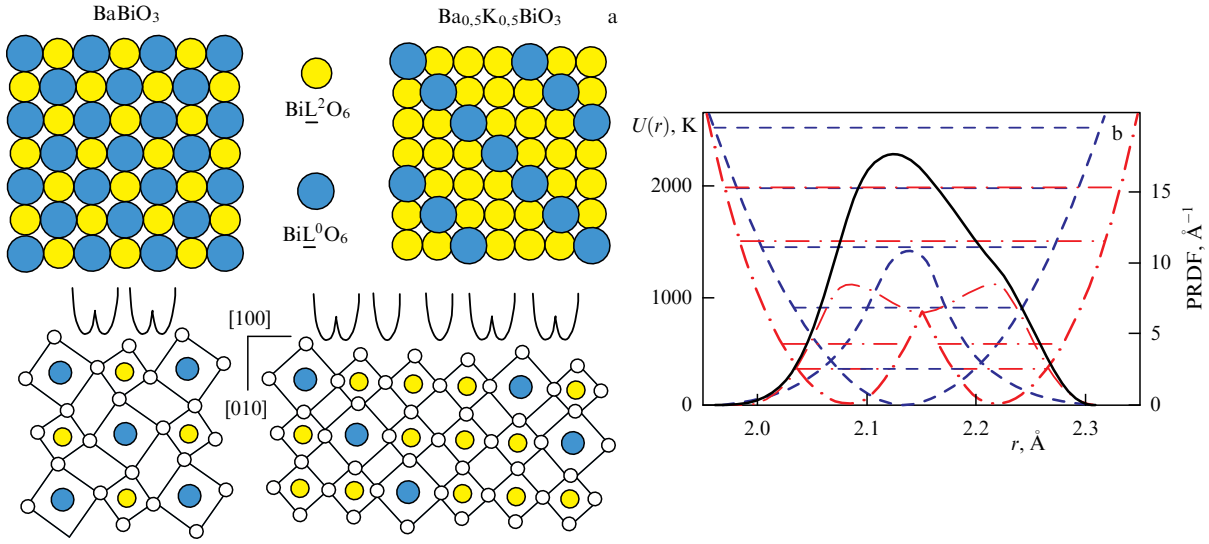

Figure 5. (a) Diagram of local crystal structure in BiO_2 plane of $BaBiO_3$ and $Ba_{0.5}K_{0.5}BiO_3$ (from [17]). At bottom, dynamical properties are shown schematically: oscillations of oxygen ions in harmonic and double-well potentials (oxygen ions are shown by small circles). (b) Pair radial distribution function of atoms together with double-well and harmonic potentials of oxygen ion oscillations in $Ba_{1-x}K_xBiO_3$ (from [10]).

Different electron filling of the upper Bi6s–O2p$_{\sigma^*}$ antibonding orbital of neighboring rigid and soft octahedra arises solely due to the pairing of electrons and holes on neighboring octahedra, which allows local electron pairs to tunnel between neighboring nonequivalent rigid BiL^2O_6 and soft BiL^0O_6 octahedra, in accordance with the dynamical exchange $BiL^0O_6 \leftrightarrow BiL^2O_6$.

As the results of our low-temperature EXAFS studies [9, 10] showed, the tunneling of local pairs causes oscillations of oxygen ions connecting different octahedra in an anharmonic double-well potential at low temperature (Fig. 4a).

At the same time, in the $BaPbO_3$ compound, where lead has one less electron than bismuth, local electron pairs do not arise, and two neighboring PbL^2O_6 octahedra have identical free levels on the upper antibonding Pb6s–O2p$_{\sigma^*}$ orbital and are identical rigid complexes. In this case, tunneling is absent, and only a standard harmonic potential of oscillations of oxygen ions connecting identical octahedra is observed in the system (Fig. 4b) [10].

Doping $BaBiO_3$ with potassium is equivalent to hole doping and leads to a partial replacement of larger soft BiL^0O_6 octahedra with smaller rigid BiL^2O_6 octahedra [10]. This leads to a decrease in and ultimately the disappearance of static breathing and rotational distortions; the lattice must compress despite the practically equal ionic radii of K^+ and Ba^{2+}. As a result, according to neutron diffraction data [50], the crystal structure becomes simple cubic at the doping level $x \geqslant 0.37$ (Fig. 5a). However, locally sensitive EXAFS studies showed an important difference between the local dynamical crystal structure and the average (static) one: oxygen ions belonging to different neighboring BiL^0O_6 and BiL^2O_6 octahedra continue to oscillate in a double-well potential, as in $BaBiO_3$, whereas those connecting two identical BiL^2O_6 octahedra oscillate in a simple harmonic potential [10], as in $BaPbO_3$ (Fig. 5b).

Importantly the features of the local crystal structure and (static and dynamical) lattice distortions that violate translation symmetry and demonstrate significant differences from the average one appear only in probing methods sensitive to local structure, such as XPS (X-ray photoelectron spectroscopy) [25], Raman scattering [51, 52], and EXAFS [9, 10].

4. Direct experimental evidence of initially paired state of charge carriers in $BaBiO_3$

We emphasize that our bond disproportionation model agrees well with the results of X-ray and neutron diffraction, inelastic neutron and electron scattering, Raman light

scattering, and photoemission spectroscopy. Given the preservation of real-space pairing occurring when doping the initial $BaBiO_3$ with potassium [10, 52], it allowed proposing a new scenario for the microscopic superconductivity mechanism in $Ba_{1-x}K_xBiO_3$ (BKBO) based on the existence of a spatially separated Fermi–Bose mixture [15–17].

However, our EXAFS and resonant Raman scattering results [9, 10, 52], as well as the results of optical conductivity measurements, Raman light scattering, and transport properties previously cited in [21], can only be regarded as indirect evidence of local pairing of charge carriers in the $BaBiO_3$ ground state. Therefore, we set the task of obtaining direct experimental evidence of the existence of an initially paired state of charge carriers in $BaBiO_3$.

In recent years, X-ray free-electron lasers (XFELs) have opened up unique opportunities for time-resolved studies of charge ordering dynamics and the relation between electron, spin, and lattice degrees of freedom in complex systems such as cuprate HTSCs [53–56]. Photoexcitation resulting in manifestations of unique properties can be effectively separated in terms of spatial, temporal, and energy coordinates. Based on these results, we have chosen to use the unique capabilities of free-electron lasers to obtain direct evidence that the initially paired carriers in $BaBiO_3$ form a new quantum state of an LPDW.

We used tr-XAS at the oxygen *K*-absorption edge to trace the variation in the local electron structure of $BaBiO_3$ under excitation by a femtosecond laser through the optical gap. The time evolution of various electron and lattice states that we observed in the tr-XAS pump–probe experiment was unambiguously indicative of the existence of local electron and hole pairs in the $BaBiO_3$ ground state.

We studied time-resolved X-ray absorption spectra at the oxygen *K*-absorption edge under resonant photoexcitation of $BaBiO_3$ thin films with a thickness of 90 nm grown on Si membrane substrates with a thickness of 100 nm. The experiment was carried out at the Spectroscopy and Coherent Scattering (SCS) beamline of the EuXFEL. All measurements were performed at room temperature [14].

Figure 6a shows the pump–probe tr-XAS experiment on $K-O$ absorption spectroscopy of $BaBiO_3$ using transmission zone plates in combination with a diffraction grating (TZPG) under pumping by an optical laser with a wavelength of 633 nm. After splitting, half of the X-ray beam passed through the $BaBiO_3$ thin-film sample, which was irradiated by a femtosecond (30 fs) optical laser pulse, and the other half, through a nonirradiated sample. To measure the spectra, a unique ultra-fast detector, DSSC (DEPFET sensor with signal compression), with a frame refresh rate up to 4.5 MHz was used, which allowed fully synchronizing the detector with the X-ray laser and measuring the scattering pattern from each pulse individually. The DSSC detector simultaneously recorded the full spectrum of the sample in the initial state, the spectrum of the sample under resonant optical pumping excitation, and the difference spectrum between the excited and ground states. The synchronization system allowed obtaining information in a wide range of delays between the optical and X-ray laser pulses: −0.1, 0, 0.2, 1, 2, 5, 10, and 60 ps.

The sample was excited by laser pulses with a duration of 30 fs with a photon energy of 1.96 eV (633 nm) and a pump fluence up to 32 mJ cm^{-2}. The energy of the probing X-ray photon was scanned in the region of the oxygen *K*-absorption edge in the range of 525–550 eV [57] with an energy resolution $\Delta E/E \sim 2 \times 10^{-4}$. In this way, we directly investigated the change and dynamics of the density of $BaBiO_3$ free states after femtosecond exposure to an exciting laser pulse through the optical gap $E_G \approx 1.96$ eV.

XAS spectra at the oxygen *K*-absorption edge of the ground and excited states of $BaBiO_3$ are shown in Fig. 6b. They consist of a pre-edge peak in the range of 529 eV, which arises under excitation to free states of the antibonding Bi6s–$O2p_{\sigma^*}$ orbital (the region shown in red in Fig. 6b), a shoulder in the range of 531–533 eV corresponding to hybridized O2p–Bi6p states (green region), and the main peak at 533–535 eV, which is mainly determined by hybrid states O2p–Ba5d (blue region) [25, 58].

The bottom panel of Fig. 6b shows the difference spectra between the excited state spectra measured at a pump laser energy density of 8 mJ cm^{-2} and the ground-state spectra for different delay times between the pump and probe pulses from −0.1 to 59.8 ps. We can immediately see positive and negative peaks appearing in the pre-edge region of the difference spectrum ΔXAS after excitation, which corresponds to an increase and decrease in XAS intensity on the rising edge and near the center of the pre-edge peak, respectively.

These positive and negative contributions to ΔXAS, which we call peaks A and B in what follows, are separated by ~ 1 eV in energy and are already visible at 0 ps, demonstrating maximum amplitude at ~ 0.2 ps, followed by a monotonic decay. We note that, during the first picosecond, 0–0.8 ps after excitation, the A peak maximum shifts by ~ 0.2 eV towards higher energies. This shift is shown in more detail in Fig. 6c, d.

The difference spectrum also contains several less pronounced negative and positive features in the energy region of 531–533 eV. They become clearly visible at a delay time of 0.1 ps and undergo intensity redistribution during the first picosecond after excitation, with the negative feature disappearing shortly after 0.5 ps. At long delay times, the amplitudes of the remaining features change insignificantly.

In the energy range of 533–535 eV of the difference spectrum, no features are visible near zero time. But at delay times of 0.2–0.3 ps, two weak minima appear in this range. Their amplitudes continue to increase slowly and reach saturation between 0.8 and 1.8 ps. Importantly, most of the described spectral features do not disappear completely until the longest delay time of 59.8 ps is reached in our experiment. This indicates that the system does not relax to the ground state at least until 60 ps after excitation into a new quasiequilibrium state.

We believe that the most important information about the rearrangement of the local electron and crystal structure under excitation through the optical gap in $BaBiO_3$ is contained in the pre-edge XAS region, because this very energy range corresponds to excitation to free states of the upper Bi6s–$O2p_{\sigma^*}$ antibonding orbital.

The dependence of the shape of the pre-edge peak on the delay time after resonant optical excitation manifests itself in the difference spectrum as a change in the amplitudes, positions, and widths of the A and B peaks (Fig. 6b). This allows analyzing the entire dynamics of the local rearrangement of the electron and crystal structure in $BaBiO_3$. The analysis is therefore mostly focused on this spectral range of the density of free states of $BaBiO_3$ after femtosecond

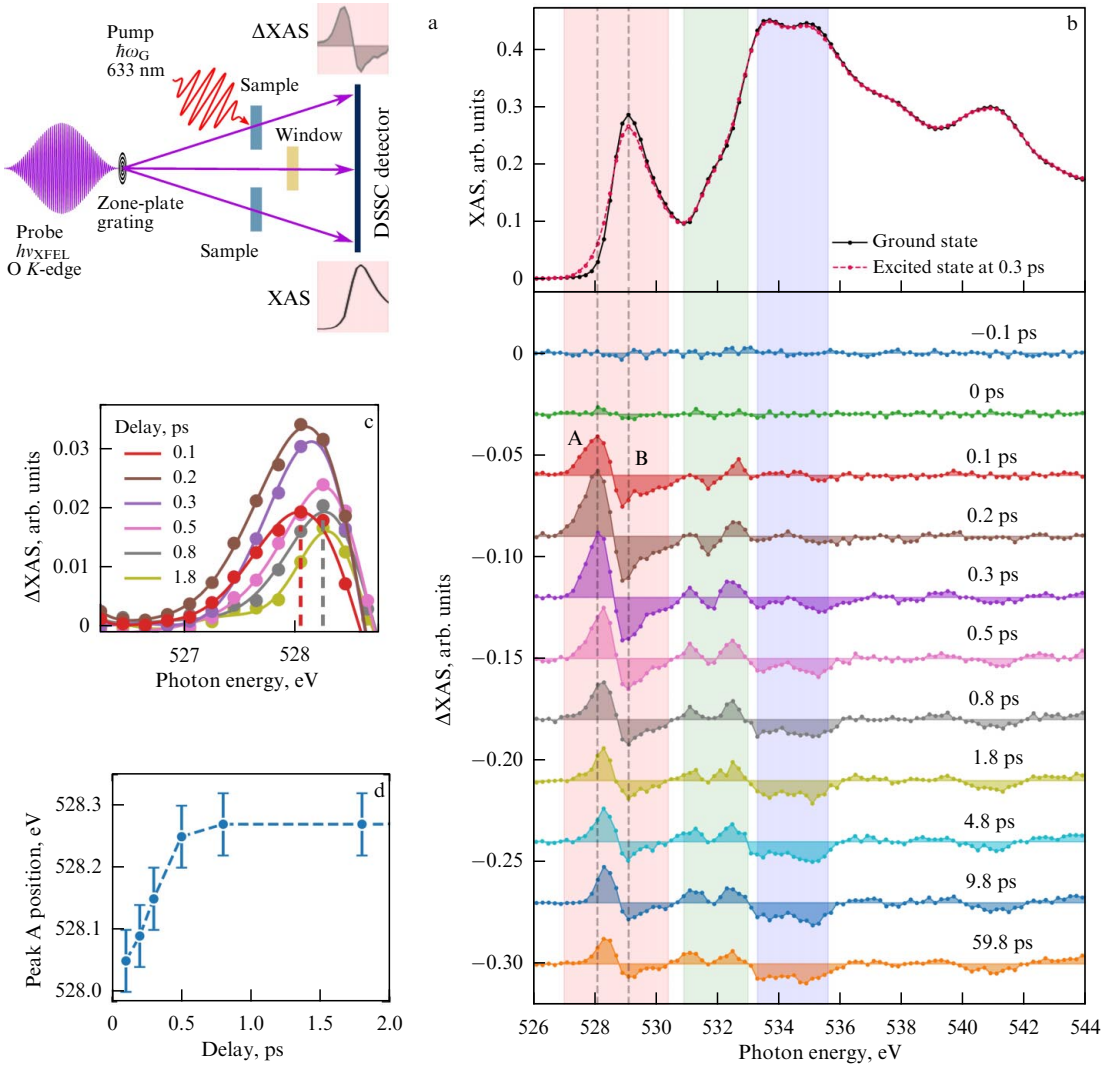

Figure 6. Pump–probe tr-XAS experiment with European X-ray Free-Electron Laser EuXFEL with $BaBiO_3$ at oxygen *K*-edge with femtosecond resolution. (a) Schematic of tr-XAS experiment at SCS beamline, where DSSC is X-ray imager with megapixel camera and with single-photon resolution. (b) Upper panel: experimental O−*K* XAS spectrum of ground (black line) and excited (red line) states of $BaBiO_3$, measured at delay time of 0.3 ps and optical pump fluence of 8 mJ cm^{-2}. Three characteristic spectral ranges are marked with colors: red, pre-edge O−*K* XAS peak corresponding to antibonding orbital Bi6s–O2p$_{\sigma^*}$; green, rising edge of main O−*K* XAS peak corresponding to hybridized states O2p–Bi6p; blue, main O−*K* XAS peak corresponding to hybridized states O2p–Ba5d (lattice states). Lower panel: difference spectra of excited and ground states ΔXAS of $BaBiO_3$, measured at different delay times ranging from −0.1 to 59.8 ps. Positive peak A and negative peak B in ΔXAS are marked with vertical dashed line. (c) Evolution of peak A in ΔXAS with delay time ranging from 0.1 to 1.8 ps. (d) Energy position of peak A versus delay time (from [14]).

excitation by a laser pulse through the optical gap $E_G \approx 1.96$ eV.

The evolution of the pre-edge peak of the oxygen *K*-edge XAS on the delay time at different optical pump fluences is shown in Fig. 7a–c. The maximum variation in the pre-edge peak is observed at a short delay (0.2 ps) after excitation: the peak broadens and shifts towards lower photon energies, and its amplitude significantly decreases.

At later delay times (0.8–4.8 ps), the peak restores its amplitude and shifts back to higher photon energies, although not entirely, indicating the transition of the system to a new excited metastable state. Notably, the shape of the peak at 4.8 ps is close to the shape at 0.8 ps. This means that the rearrangement of the local electronic and crystal structure is basically completed already at a delay time of 0.8 ps. As the excitation fluence increases, similar effects are qualitatively observed in the pre-edge region, but they are more pronounced.

At times $\geqslant 0.8$ ps after excitation, the sample can be characterized as a mixture of the excited and ground states of $BaBiO_3$, with the density of states (DOS) of each type contributing to XAS with a certain weight. Figure 7d–f shows spectra measured at a delay time of 4.8 ps, taking the sum of the *ab initio* DOS for the ground and excited states into account.

The $BaBiO_3$ ground state is characterized by a monoclinic distortion of the ideal cubic perovskite lattice and two types of oxygen octahedra. In the excited state, the octahedra become identical and the lattice distortion disappears. The parameters of the ground state contribution to XAS (energy position and width) were found by approximating the nonexcited spectrum. The energy position of the excited state contribution to XAS was determined from the energy separation between the peak and the dip in the difference spectrum (Fig. 6b). The weight of the excited state α was obtained from the spectra using the equation XAS =

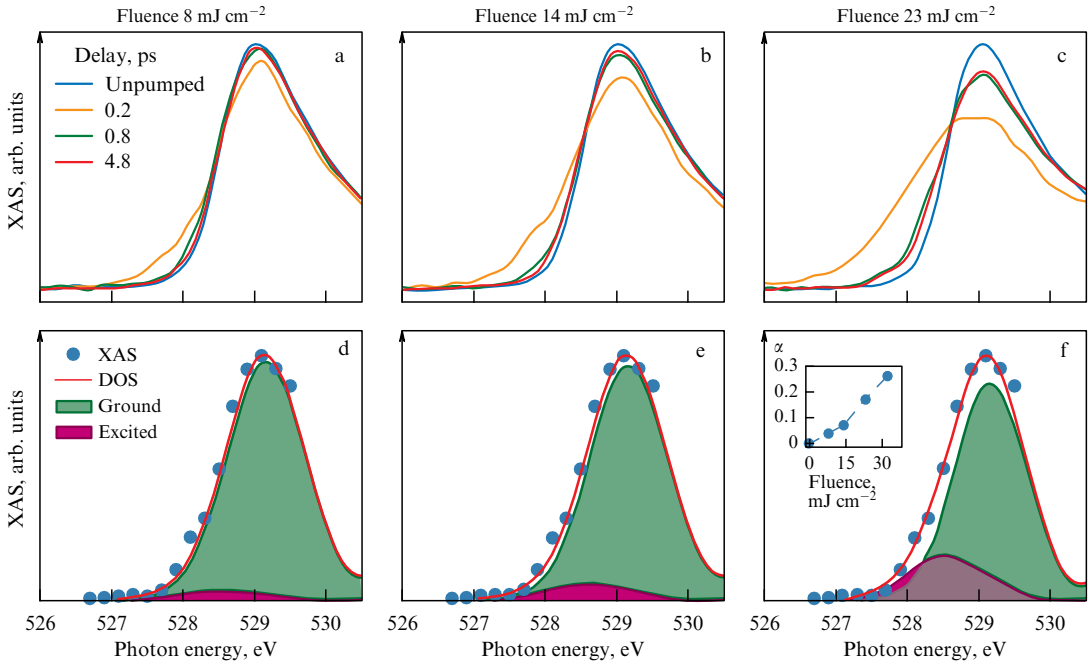

Figure 7. Dynamics of pre-edge peak in $K-$O XAS spectrum corresponding to excitation into region of free states of Bi6s–O2p$_{\sigma^*}$ orbital of $BaBiO_3$. (a–c) Pre-peak O$-K$ XAS edge of $BaBiO_3$, measured in ground and excited states at different delay times after excitation (0.2, 0.8, and 4.8 ps) at three optical pump fluences. (d–f) Experimental pre-edge XAS peak at delay time of 4.8 ps (blue dots) and its fit (solid red line) by sum of calculated DOS of ground (green) and excited (purple) states. Inset in Fig. f: fraction of excited state α in resulting XAS spectrum versus optical pump fluence (from [14]).

$(1-\alpha)\mathrm{DOS}_{\mathrm{ground}} + \alpha\mathrm{DOS}_{\mathrm{excited}}$. It shows an almost linear dependence on the optical pump fluence (the inset in Fig. 7f). At the maximum optical pump density of 32 mJ cm^{-2} used in our experiment, the fraction of the excited state reaches 27%. To reduce the thermal load and prevent damage to the thin-film sample, most time-resolved measurements were performed at a pump energy density of 8 mJ cm^{-2}, at which the excited state fraction is estimated as 5%.

To estimate the characteristic times of rearrangement of the local electron and crystal structure in $BaBiO_3$ after femtosecond resonant excitation through the optical gap, we used a three-exponential model [54]. Figure 8 shows the results of scanning the A peak shape versus the delay time in the ΔXAS difference spectrum, obtained at a fixed photon energy of 528.2 eV, and this dependence is fitted by three exponentials in accordance with the equation

$$\Delta\mathrm{XAS} = \left[\Theta(t-t_\mathrm{d})\left(1-\exp\left(-\frac{t-t_\mathrm{d}}{\tau_1}\right)\right)\right.$$
$$\left.\times\left(A_1 + A_2\exp\left(-\frac{t-t_\mathrm{d}}{\tau_2}\right) + A_3\exp\left(-\frac{t-t_\mathrm{d}}{\tau_3}\right)\right)\right]^2.$$

As a result of the fitting, three characteristic times are obtained, which we attribute to the rapid excitation of the electron subsystem immediately after absorption of the laser pulse, $\tau_1 \sim 0.15$ ps; relatively fast partial relaxation of the electron subsystem back to the ground state, $\tau_2 \sim 0.24$ ps; and slower lattice rearrangement, $\tau_3 \sim 1.5$ ps.

We note once again that the amplitudes of both the A and B peaks in Fig. 6b do not relax to zero at long delay times, which confirms the formation of a new state of the system after excitation, stable for at least tens of picoseconds.

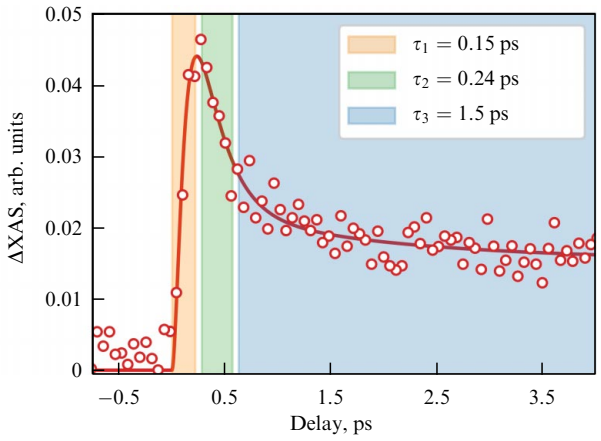

Figure 8. Three-exponential approximation of time dependence of ΔXAS at photon energy of 528.2 eV (peak A). Red circles: delay time scan measured at fixed photon energy of 528.2 eV, which corresponds to peak A in difference spectrum ΔXAS and pump fluence of 8 mJ cm^{-2}. Solid red line: three-exponential approximation of time scan. Time intervals in which three characteristic processes making main contributions are marked with colors: orange, electron structure excitation; green, electron structure relaxation; and blue, lattice rearrangement. Inset: three characteristic times obtained as result of exponential approximation (from [14]).

The time dependence of the ΔXAS difference spectrum (Fig. 6b, c) during the first picosecond after resonant optical excitation provides direct confirmation that charge carriers in the ground state of $BaBiO_3$ exist in the form of electron and hole pairs respectively localized in large and small octahedral complexes. Based on the general assumption about such conditions, which we describe in detail below, the features of the difference spectra in the pre-edge region of XAS can be

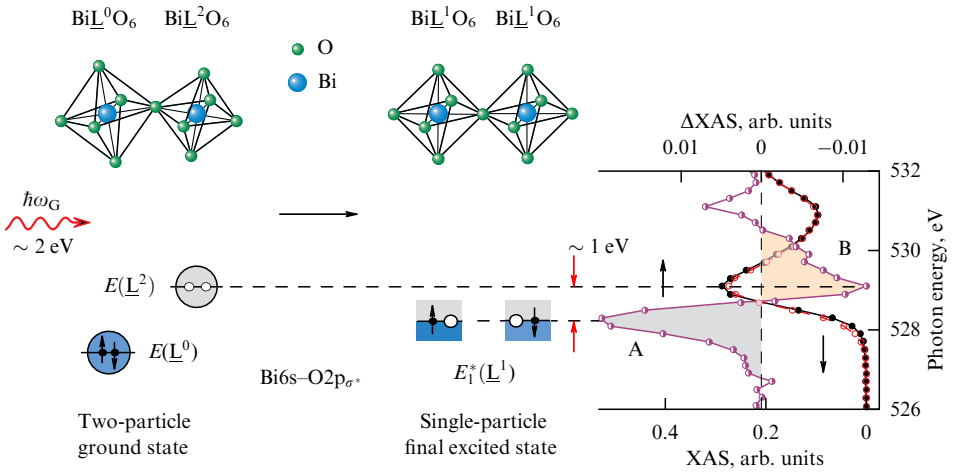

Figure 9. Schematic of excitation of ground state of $BaBiO_3$ by resonant optical photon. Main changes occurring in $BaBiO_3$ under rapid resonant excitation through optical gap. Simultaneous rearrangement of local electron (lower panel) and local crystal (upper panel) structures is reflected in shape of oxygen *K*-edge XAS and ΔXAS difference spectrum of $BaBiO_3$ at delay time of 0.8 ps (right panel) (from [14]).

associated with contributions from paired and single-electron hole states before and after excitation [10].

As can be seen from Fig. 6b–d, the energy position of peak A in the difference spectrum stabilizes at a delay time of 0.8 ps after the arrival of the laser pulse. This suggests that the process of local rearrangement of the electron and crystal structure in $BaBiO_3$ is practically completed by this time. Therefore, we begin the analysis of the difference spectrum from a delay time of 0.8 ps, which corresponds to reaching the final excited state. Rapid transient processes occurring at delay times of 0–0.8 ps are discussed in detail below.

In the monoclinically distorted cubic structure of the $BaBiO_3$ ground state (Fig. 9), large $Bi\underline{L}^0O_6$ and small $Bi\underline{L}^2O_6$ octahedral complexes alternate, carrying a respective local pair of electrons (shown in blue) and holes (gray) on the upper antibonding Bi6s–O2p$_{\sigma^*}$ orbital. Absorption of a femtosecond laser pulse with a photon energy resonant with the optical gap $\hbar\omega_G = E_G$ leads to the simultaneous destruction of local pairs of electrons and holes. Thus, the two-particle local electron structure with paired states $E_0(\underline{L}^0)$ and $E_0(\underline{L}^2)$ transforms into a single-particle local electron structure with two identical states $E_1^*(\underline{L}^1)$, which contain one electron and one hole at the final stage of excitation.

The two previously paired electrons from the destroyed pair are excited with an energy of ~ 1 eV to a new energy level $E_1^*(\underline{L}^1)$ in the single-particle spectrum, losing the binding energy E_b and becoming free single electrons. At the same time, two single holes $\underline{L}^1$ from the destroyed hole pair appear on the same level $E_1^*(\underline{L}^1)$, and the level $E_1^*(\underline{L}^1)$ arises approximately 1 eV below the paired hole level $E_0(\underline{L}^2)$. Such a transformation of the local electron structure causes a rearrangement of the monoclinically distorted structure of different $Bi\underline{L}^0O_6$ and $Bi\underline{L}^2O_6$ octahedra to a simple cubic structure of identical $Bi\underline{L}^1O_6$ octahedra, each containing one electron and one hole on the upper antibonding Bi6s–O2p$_{\sigma^*}$ orbital.

These changes manifest themselves in the features observed in the pre-edge region of the ΔXAS difference spectrum (see Fig. 9) at delay time $t \geqslant 0.8$ ps after laser excitation. We associate the positive peak A in ΔXAS at a lower photon energy with the single unpaired holes $\underline{L}^1$ at the energy level $E_1^*(\underline{L}^1)$ appearing as a result of local pair dissociation at the final stage of excitation, $t \geqslant 0.8$ ps. We associate the negative peak B in ΔXAS at a higher photon energy with a decrease in the density of free states on the upper antibonding Bi6s–O2p$_{\sigma^*}$ orbital of small $Bi\underline{L}^2O_6$ octahedra due to a decrease in the number of paired holes $\underline{L}^2$ at the energy level $E_0(\underline{L}^2)$.

Importantly, although the energy of the exciting photon is $\hbar\omega_G \approx 2$ eV, the separation of A and B peaks in the difference spectrum ΔXAS is ~ 1 eV. We interpret this as an imprint of the transition from a two-particle to a single-particle state of the system caused by resonant optical excitation. In this case, the quantum energy $\hbar\omega_G \approx 2$ eV necessary to break one local pair is spent on overcoming the pair binding energy E_b and exciting each of the electrons that have become free by ~ 1 eV, to a new level $E_1^*(\underline{L}^1)$ in the single-particle spectrum. Indeed, if we assume that two electrons at the $E_0(\underline{L}^0)$ level are not bound into a local pair, and the ground state represents a single-electron spectrum, then the shape of ΔXAS under resonant excitation through the CDW semiconductor gap would be different. The quantum $\hbar\omega_G \approx 2$ eV would then excite one of the two single electrons from the $E_0(\underline{L}^0)$ ground level to a vacant state in the pre-edge region at the $E_0(\underline{L}^2)$ level, and a hole would appear at the $E_0(\underline{L}^0)$ level. As a result, peaks A and B would also be observed in the ΔXAS spectrum, but the distance between them would be ~ 2 eV, which contradicts the experimental data.

Thus, the effects observed in the pre-edge region of XAS spectra at the oxygen *K*-absorption edge under resonant optical excitation should be regarded as *direct experimental proof* that $BaBiO_3$ is a unique compound with initially paired carriers forming a new quantum state of an LPDW.

In the model in [10, 15–17], local pairs of electrons and holes in neighboring octahedra are directly related. The presence of an electron pair at the $E_0(\underline{L}^0)$ energy level in a large octahedron implies the presence of a hole pair $\underline{L}^2$ at the $E_0(\underline{L}^2)$ energy level in the nearest small octahedron. The configuration of the local electron structure of the ground state of $BaBiO_3$ should then be understood as $E_0(\underline{L}^0) + E_0(\underline{L}^2)$ (see Fig. 9). Different occupations ($\underline{L}^2$ or $\underline{L}^0$) of the antibonding orbital Bi6s–O2p$_{\sigma^*}$ determine the configuration and size of the octahedron and are the main cause of breathing and rotational lattice distortions, but not vice versa, as stated, e.g., in [29, 30, 35, 36]. In the case of equal population $\underline{L}^1$ of the antibonding orbital Bi6s–O2p$_{\sigma^*}$ in the

nearest octahedra, no breathing distortion can occur, and the structure should consist of identical $Bi\underline{L}^1O_6$ octahedra (see Fig. 9).

Figure 6c, d shows the shape and energy position dynamics of peak A (the appearance and growth of the number of unpaired holes) in ΔXAS difference spectra for the delay times 0.1, 0.2, 0.3, 0.5, 0.8, and 1.8 ps. In ΔXAS, however, small precursors of peaks A and B are already observed at zero time (maximum overlap between the pump and probe pulses), and the distance between them is ~ 1 eV (Fig. 6b). This means that the process of dissociation of local pairs after absorption of an optical photon begins from a time determined by the temporal resolution in our experiment (several ten femtoseconds). At a delay time of 0.1 ps after excitation, peaks A and B already have significant amplitudes, which increase up to 0.2 ps. During a delay time of 0.1–0.8 ps, peak A shifts slightly towards higher energy by ~ 0.2 eV, and its amplitude reaches a maximum near a delay time of 0.2 ps. Within the interval of ~ 0.5–0.8 ps, the peak A position stabilizes and stops changing with a further increase in the delay time (Fig. 6d).

5. Mechanism of Bi6s–O2p-bond disproportionation and nature of pairing in $BaBiO_3$

By analyzing changes in the difference $K-O$ XAS spectra at short delay times between optical and X-ray laser pulses [13, 14], we could obtain comprehensive information about the mechanism of Bi6s–O2p-bond disproportionation and the nature of charge carrier pairing in $BaBiO_3$ (Fig. 10).

The first stage of excitation after absorption of a resonant ($\hbar\omega_G = E_G \approx 2$ eV) optical pump pulse at delay times of 0–0.3 ps corresponds to the transformation from a two-particle (Fig. 10a) to a single-particle (Fig. 10b) spectrum. At this stage, both local pairs of electrons and holes dissociate simultaneously with a characteristic time τ_1 (Fig. 10b) in accordance with the optical transition $E_0(\underline{L}^0) + E_0(\underline{L}^2) \rightarrow E_2^*(\underline{L}^0) + E_2^*(\underline{L}^2)$. This transforms the two-particle energy level structure into a new single-particle one, where $E_2^*(\underline{L}^0)$ and $E_2^*(\underline{L}^2)$ are intermediate excited single-particle levels with two unpaired electrons and two unpaired holes in the large and small octahedra, respectively, in the intermediate excited state $|2\rangle$.

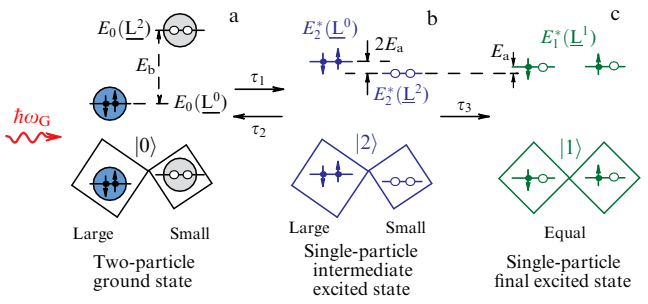

Figure 10. Diagram of rapid transient processes occurring in $BaBiO_3$ at short delay times after excitation. Detailed schematic of rearrangement of local electron structure of $BaBiO_3$ (top) and local crystal structure (bottom), observed at delay times of 0–0.8 ps after femtosecond resonant excitation through optical gap $\hbar\omega_G = E_G$. (a) Two-particle paired ground state $E_0(\underline{L}^0) + E_0(\underline{L}^2)$; (b) single-particle unpaired intermediate excited state $E_2^*(\underline{L}^0) + E_2^*(\underline{L}^2)$; (c) single-particle metastable final excited state $2E_1^*(\underline{L}^1)$ (from [14]).

Thus, the energy of both electrons increases by $\hbar\omega_G/2 = E_b/2 + E_a \approx 1$ eV relative to the initial level $E_0(\underline{L}^0)$, and the energy of the $E_2^*(\underline{L}^2)$ level with two unpaired holes shifts by the same amount $\hbar\omega_G/2$ in the opposite direction relative to the initial position $E_0(\underline{L}^2)$. An activation gap $2E_a$ appears between the $E_2^*(\underline{L}^0)$ and $E_2^*(\underline{L}^2)$ levels. Importantly, at the first stage of excitation, two unpaired electrons and two unpaired holes remain in their octahedra, while maintaining the breathing distortion of the lattice due to the persistent different occupation ($\underline{L}^2$ and $\underline{L}^0$) of the antibonding orbital Bi6s–O2p$_{\sigma^*}$.

Until the lattice has rearranged, the intermediate excited state $|2\rangle$ can relax back to the ground state. This process with a characteristic time τ_2 occurs as a reverse transition $E_2^*(\underline{L}^0) + E_2^*(\underline{L}^2) \rightarrow E_0(\underline{L}^0) + E_0(\underline{L}^2)$, which is likely accompanied by the emission of a photon with energy $\hbar\omega \sim 2$ eV, returning the pairing energy E_b to the system.

The first stage of excitation with a characteristic time τ_1 is observed in the ΔXAS difference spectrum at delay times of 0–0.3 ps as the simultaneous appearance and growth of peak A (appearance and increase in the number of unpaired holes at the $E_2^*(\underline{L}^2)$ level) and negative peak B (decrease in the number of paired holes at the $E_0(\underline{L}^2)$ level), proportional to the number of destroyed pairs. The recombination process into the initial paired state with a characteristic time τ_2 becomes noticeable after ~ 0.2 ps as a slight decrease in the amplitudes of A and B peaks.

At delay times of 0.3–0.8 ps after excitation, the dominant process is given by the transformation of the local electron structure with the levels $E_2^*(\underline{L}^0)$ and $E_2^*(\underline{L}^2)$, belonging to different octahedra and respectively occupied by two unpaired electrons and two unpaired holes, into a structure with two half-filled singlet $E_1^*(\underline{L}^1)$ levels, corresponding to identical octahedra (the final excited state $|1\rangle$). This transition of one of the electrons of the large octahedron to a small neighboring one, described by the equation $E_2^*(\underline{L}^0) + E_2^*(\underline{L}^2) \rightarrow 2E_1^*(\underline{L}^1)$, causes a lattice rearrangement into an ideal cubic structure with identical octahedra. This process is accompanied by the closure of the activation gap $2E_a$ and is characterized by the time τ_3 (Fig. 10c).

In the difference spectrum ΔXAS, this stage at delay times of 0.3–0.8 ps should be observed as a shift of peak A towards higher energies by the value E_a due to the transformation of level $E_1^*(\underline{L}^2)$ into levels $E_1^*(\underline{L}^1)$ (transition $\underline{L}^2 \rightarrow 2\underline{L}^1$). Indeed, taking $E_a \approx 0.24$ eV from [21], we obtain an exhaustive explanation for the shift of peak A by ~ 0.2 eV, observed in the difference spectrum ΔXAS (Fig. 6c, d).

After reaching the final excited state $|1\rangle$, the electron transition $2E_1^*(\underline{L}^1) \rightarrow E_0(\underline{L}^0) + E_0(\underline{L}^2)$ with a return to the ground state $|1\rangle \rightarrow |0\rangle$ is forbidden, because this requires an energy of $2E_a$ for the reverse lattice rearrangement. Thus, in the final state $|1\rangle$, the system has a structure of identical octahedra with a half-filled antibonding orbital Bi6s–O2p$_{\sigma^*}$ and is metastable for up to 60 ps at least.

The slow monotonic decrease in the amplitudes of peaks in the difference spectrum at long delay times 0.8–60 ps (Fig. 6b) indicates that the excited state of the system tends to relax to the ground state over a very long time compared to the time scales of our experiment. This relaxation is likely to occur due to the interaction of the initially optically excited volume of the sample with the surrounding nonexcited matrix. We note that the fraction of the excited state in the probed volume does not exceed 5% at a pump fluence of 8 mJ cm^{-2} (see Fig. 7).

Given the fitting of the ΔXAS difference spectrum at the peak A energy using a three-exponential model (see Fig. 8) and fast transient processes observed at a delay of 0–0.8 ps (see Fig. 10), we can estimate the characteristic time of destruction of local electron and hole pairs by resonant femtosecond excitation through the optical gap as $\tau_1 = 0.15$ ps, the pair recombination time (relaxation to the ground paired state) as $\tau_2 = 0.24$ ps, and the time of lattice rearrangement into a simple cubic structure with identical octahedra as $\tau_3 = 1.5$ ps.

The relatively large characteristic time at the first stage of excitation, estimated as $\tau_1 \sim 0.15$ ps (see Fig. 8), can be considered yet another argument in favor of the two-particle system of the $BaBiO_3$ ground state. Indeed, in the case of a single-particle spectrum, the time of excitation of a single electron upon absorption of a photon with energy $\hbar\omega_G \approx 2$ eV is on a femtosecond scale, and hence a faster process close to the laser pulse duration should be observed in the spectrum. Apparently, the destruction of the paired state is a more complex process than the excitation of a single electron, requiring additional energy and time.

Thus, the first direct observation of the rapid processes of dissociation of electron and hole pairs, accompanied by lattice rearrangement at short delay times of 0–0.8 ps (see Fig. 10), is another very important fundamental result in this paper. It directly demonstrates the nature of the two gaps in $BaBiO_3$ and indicates that, under femtosecond resonant optical excitation, carrier pairing and Bi6s–O2p bond disproportionation disappear, and the optical and activation gaps close.

The last effect is a signature of an insulator–metal phase transition, and therefore the system with a cubic structure and identical octahedra should exhibit metallic properties in the final excited state $|1\rangle$, like the hypothetical $BaBi^{4+}O_3$ system [23, 59], which agrees well with the results of our calculations by the DFT method [60].

In addition, we note that the density of states of paired local ligand holes $\underline{L}^2$ in the two-particle spectrum (Fig. 10a), which in the ground state XAS manifests itself as a pre-edge peak (Fig. 6b), transforms into the density of vacant single states $\underline{L}^1$ in the single-particle spectrum under resonant excitation through the optical gap (Fig. 10c) and forms a conduction band in the metallic metastable excited state.

The existence of two energy gaps in $BaBiO_3$ was previously interpreted in a number of studies [21, 39, 61, 62], but here we show directly that the optical gap is determined by the energy needed to overcome the pairing energy and the activation energy: $E_G = E_b + 2E_a$. The pairing energy E_b is responsible for binding the electrons and holes located on completely filled and unoccupied levels in the respective large and small octahedra into local pairs. It is the pairing energy E_b that provides the energy gain and makes the bond disproportionation process in $BaBiO_3$ energetically advantageous. The activation energy E_a is associated with breathing and rotation types of cubic lattice distortion, manifesting as a monoclinically distorted structure with different octahedra. The activation gap $2E_a$ is an energy barrier in the two-particle spectrum that prevents two-particle charge transfer in a structure with different octahedra and disappears under the transformation of the lattice into a system with identical octahedra, causing an insulator–metal transition. As we have noted, the activation gap plays the role of pair localization energy in two-particle charge transfer [10, 15, 17].

The extremely large value of the preexponential factor in transport measurements $n(T) = n_0 \exp(-E_a/kT)$, where $n_0 = 1.1 \times 10^{22}$ cm^{-3} is equal to the concentration of unit cells [21], becomes evident because we have shown that each unit cell in $BaBiO_3$ carries a local pair and participates in two-particle conductivity.

In addition, the nature of the extremely large amplitude of the breathing Raman mode at ~ 570 cm^{-1} in Raman light scattering spectra [21, 51] under resonant excitation through the optical gap is clarified. The rupture of charge carrier pairs leads to the closure of the activation gap and rapid (0.8 ps) local structural rearrangement. The energy $2E_a$ released during shock local lattice deformation causes an anomalous increase in the intensity of the breathing Raman mode of ~ 570 cm^{-1}, which allows experimentally observing its higher harmonics up to the fifth order in Raman light scattering spectra [21, 51].

Importantly, the analysis of fast transient processes at delay times of 0–0.8 ps (see Fig. 10) provides an entirely new experimental insight into the mechanism of Bi6s–O2p bond disproportionation in $BaBiO_3$. This casts doubt on earlier conclusions based on DFT calculations that either the breathing mode regime [29] or the different local environment of Bi atoms in $BaBiO_3$ [30] is responsible for bond disproportionation. Our experiment shows that the local electron and crystal structure of the final excited state (Fig. 10c), corresponding to the cubic lattice of the hypothetical $BaBi^{4+}O_3$ system, cannot transform into a structure with breathing distortion with large and small octahedra (Fig. 10b) by a simple change in the local environment of the Bi atom, i.e., the transition of one of the ligand holes $\underline{L}^1$ to the neighboring octahedron ($\underline{L}^1 \rightarrow \underline{L}^2$), because this would require energy costs of $2E_a$. Such a transition becomes energetically advantageous only if two electrons and two holes form local pairs in the respective large and small octahedra, releasing the binding energy E_b (Fig. 10a). Thus, the *mechanism* of Bi6s–O2p-bond disproportionation in the $BaBiO_3$ ground state results only from the *local pairing* of electrons and holes *in real space*, and the observed monoclinic lattice distortion is a direct consequence of local pairing [13, 14].

Another major consequence deduced from the scheme of fast transient processes occurring at short delay times, presented in Fig. 10, is the possibility of clarifying the nature of local pairing of electrons and holes in $BaBiO_3$. Indeed, the transition from a more energetically advantageous ideal cubic structure to a monoclinically distorted lattice (from Fig. 10c to Fig. 10b) requires energy costs of $2E_a$ and at this stage prevents the system from attaining the ground state with minimum energy and paired charge carriers (Fig. 10a). Thus (in contrast to the Bardeen–Cooper–Schrieffer (BCS) theory), lattice deformation serves to not facilitate but hinder the pairing process. In view of the very large scale of the pairing energy $E_b \approx 1.5$ eV and the very small time scale of local pair destruction, 150 fs, and reverse relaxation, 240 fs, into the paired state unattainable in the phonon subsystem, we conclude that the pairing mechanism in $BaBiO_3$ cannot have a phonon (bipolaron) nature, and we are dealing with a manifestation of the electron nature of local charge carrier pairing in real space [13], as was assumed, e.g., in [2, 38, 39].

This possibility was also confirmed by Geballe [63], who pointed to the family of HTSCs based on $BaBiO_3$ as the first example of experimental confirmation of the existence of Anderson's negative potential [3].

At the same time, one cannot rule out the possibility of realizing a dynamical pairing mechanism in which the lattice can play an indirect role, facilitating the pairing process through a dynamical contribution, for example, in the form of oscillations of oxygen atoms in a double-well potential [13].

Introducing the concept of an LPDW as a new quantum state of charge carriers in $BaBiO_3$, we use the local character of the CDW [1, 31] but emphasize the high importance of charge carrier pairing and a strong localization of electron and hole pairs in real space on different octahedra of the crystal structure.

For a conventional CDW, charge carriers do not necessarily have to be in a paired state, and the LPDW is formed due to the alternation of local pairs of electrons and holes in neighboring octahedra. Besides, this definition shows the difference between such an LPDW and the PDW state recently discovered in cuprate HTSCs [64]. Indeed, a PDW in cuprates describes a wave of paired carriers in momentum space, whereas the LPDW is strictly related to local pairing of electrons and holes in real space.

Moreover, the LPDW state has a dynamical character due to local pair tunneling between neighboring complexes in accordance with the dynamical exchange $Bi\underline{L}^2O_6 \leftrightarrow Bi\underline{L}^0O_6$, which causes oscillations of the oxygen atom in a double-well potential [10]. The LPDW state with alternating local pairs of electrons and holes means that the charge difference between neighboring octahedra is exactly $2e$.

A similar phenomenon of real-space pairing was previously discussed for cuprate HTSCs, $SrTiO_3$, and related compounds with a perovskite-like structure in the form of the appearance of a pre-pairing state preceding the formation of a superconducting state [65–67]. For example, in Zr-doped $SrTiO_3$, where the existence of unconventional pairing in real space was predicted in [68], pre-formed local electron pairs can be viewed as a precursor to a superconducting Bose–Einstein condensate (BEC) at lower temperatures and in weaker magnetic fields. In the BEC regime, the pairing has a local character and precedes the formation of a superconducting state [67].

Thus, our unique tr-XAS experiment at the EuXFEL with femtosecond resonant laser excitation through the optical gap directly indicates the existence of local pairs of electrons and holes in the ground state of $BaBiO_3$.

We were the first to experimentally observe the transformation of the spectrum of an initially two-particle system into the spectrum of a single-particle ensemble of free charge carriers.

We see that, after excitation, the system does not relax to the initial state for at least 60 ps (the maximum delay time in our experiment). Instead, it remains in a new quasiequilibrium state with a structure of identical octahedra. Because both optical and activation gaps close shortly after the excitation, this metastable state is likely to behave like a metal with a half-filled valence band, similarly to the hypothetical $BaBi^{4+}O_3$ system.

Changes in the XAS spectrum of $BaBiO_3$ under resonant laser excitation through the optical gap can hardly be explained using a single-electron approach, but they can be interpreted much more consistently as a result of dissociation of charge carrier pairs. This suggests that the ground state of $BaBiO_3$ is not a conventional CDW but a new quantum state of an LPDW.

Changes observed in XAS at short delay times from 0 to 0.8 ps allowed identifying the characteristic times of local pair dissociation ($\tau_1 = 0.15$ ps), recombination into the initially paired state ($\tau_2 = 0.24$ ps), and lattice rearrangement from a monoclinic structure with breathing and rotational distortions to an ideal cubic structure with identical octahedra ($\tau_3 = 1.5$ ps).

Analysis of the intermediate phase of excitation provided an absolutely new experimental insight into the mechanism of Bi6s–O2p-bond disproportionation and allowed making an important conclusion regarding the manifestation of the electron nature of local charge real-space pairing of the carriers $BaBiO_3$ [13].

6. Formation of Fermi–Bose mixture in $Ba_{1-x}K_xBiO_3$

The results of the experiment at EuXFEL also allow a deeper understanding of the local processes occurring in $BaBiO_3$ upon doping with potassium, as we described earlier in the model of a spatially separated Fermi–Bose mixture explaining the superconductivity mechanism in bismuthates; these processes are schematically presented in Fig. 11, where bosonic and fermionic contributions to the two- and single-particle density of states are shown separately.

In the absence of doping at $x = 0$, the filled and free bosonic bands present in the two-particle system are separated by a transport (activation) gap $2E_a$, which prevents free motion of local pairs in space. This state can be considered a two-particle (bosonic) analogue of a conventional semiconductor with a band gap $2E_a$ and a bosonic chemical potential μ_0 at the center of this band.

At $x = 0$, there is no proper fermionic band, because valence $O2p_\pi$ electrons are localized on small octahedral complexes and cannot participate in conductivity due to the absence of a band of free levels above them. Therefore, a Fermi–Bose mixture is not yet formed in the parent compound $BaBiO_3$, which is a bosonic insulator (Fig. 11a).

When doping $BaBiO_3$ with potassium, replacing every two barium atoms with two potassium atoms adds two holes and replaces some of the large $Bi\underline{L}^0O_6$ octahedra with small $Bi\underline{L}^2O_6$ ones (Fig. 5a). However, these additional holes are in an unpaired state because there are no large $Bi\underline{L}^0O_6$

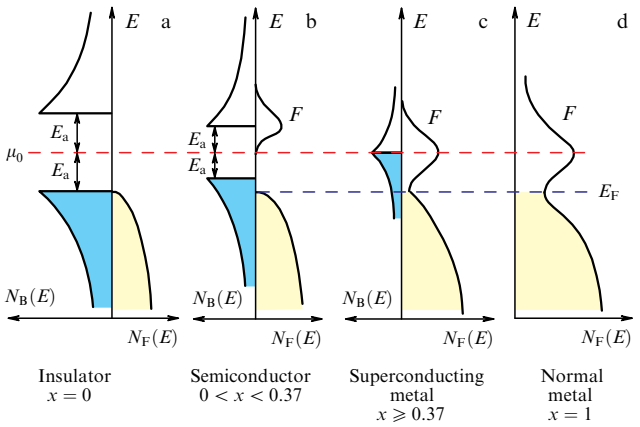

Figure 11. Schematic representation of rearrangement of local electron structure of $Ba_{1-x}K_xBiO_3$ depending on potassium doping level (from [13]). Contributions of bosonic $N_B(E)$ and fermionic $N_F(E)$ density of states are shown separately, because they are spatially separated. Filled bosonic and fermionic bands are respectively shown in blue and yellow. Unoccupied bosonic and fermionic bands have no fill. $2E_a$ is activation gap and μ_0 is chemical potential.

octahedra with paired electrons nearby. We could assume that the appearance of such unpaired states was observed in [25, 33, 58] at the oxygen *K*-absorption edge in the XAS spectrum of $Ba_{1-x}K_xBiO_3$ as a shift of the pre-edge peak by ~ 1 eV towards lower energies. This shift coincides with the shift of the unpaired hole level in the difference spectrum of the final excited state $E_1^*(\underline{L}^1)$ relative to the paired hole level $E_0(\underline{L}^2)$ in $BaBiO_3$ under resonant laser excitation (Fig. 6b; 9), which we observed in the XFEL experiment.

The appearance of a spatial overlap of small $Bi\underline{L}^2O_6$ complexes at doping level $0 < x < 0.37$ causes splitting of free $\underline{L}^2$ levels, from which a fermionic conduction band F begins to form and which are still separated by an energy gap from the valence band of $O2p_\pi$ electrons with a Fermi level E_F. The width and density of states of the fermionic F band then increase with doping due to an increase in the number of free levels proportional to the increase in the number of small octahedra $n_0(1+x)/2$ (where n_0 is the concentration of unit cells) (Fig. 11b).

In the bosonic subsystem, as the doping level x increases, the transport gap $2E_a$ decreases, facilitating the enhancement of two-particle conductivity in a bosonic semiconductor state. Although this gap decreases, it remains nonzero for $x < 0.37$ due to intersite Coulomb repulsion, which is screened inside bosonic clusters but is still effective in the space between neighboring bosonic clusters.

At the same time, the width and density of free and occupied states of the bosonic band also decrease proportionally to the decrease in the number of large octahedra $n_0(1-x)/2$. As a result, for $x < 0.37$, $Ba_{1-x}K_xBiO_3$ demonstrates a semiconductor conductivity type, which changes from simple exponential (activation) to the Mott one with a variable hopping range [69]. Thus, at low doping levels $0 < x < 0.37$, a Fermi–Bose mixture begins to form, but it is still separated both spatially and energetically (Fig. 11b).

In Figure 11c, we demonstrate the formation of a superconducting metal upon reaching and overcoming the percolation threshold $x \geqslant 0.37$, when the increase in the number of small octahedra $n_0(1+x)/2$ leads to the formation of a continuous fermionic cluster $Bi\underline{L}^2O_6$ — $Bi\underline{L}^2O_6$. At the threshold $x = 0.37$, the insulator–metal phase transition occurs simultaneously in the bosonic and fermionic subsystems. In the fermionic subsystem, free levels of small $Bi\underline{L}^2O_6$ octahedra merge into a conduction band F, which overlaps with the filled valence band of $O2p_\pi$ electrons, forming a metallic state of Fermi liquid with the Fermi level E_F.

In the bosonic subsystem, the transport gap $2E_a$ closes ($E_a = 0$) and local electron pairs in $Bi\underline{L}^0O_6$ octahedra delocalize but do not disappear due to the preservation of the binding energy $E_b = E_G \approx 0.5$ [52]. The spatial motion of local pairs becomes free, ensuring the state of a bosonic superconducting metal shunted by a fermionic component. As a result, for $x \geqslant 0.37$, a spatially separated Fermi–Bose mixture is formed in the system [15–17] (Fig. 11c).

Apparently, the normal metallic conductivity in BKBO is largely due to the fermionic contribution. At the same time, a bosonic contribution was also observed in the experiments of Hellman and Hartford [70], where it manifests itself as two-particle tunneling in the normal state.

A further increase in the doping level should lead to the loss of the superconducting properties of the compound as a result of the complete replacement of large $Bi\underline{L}^0O_6$ octahedra with small $Bi\underline{L}^2O_6$ octahedral complexes. Local electron pairs disappear, the bosonic subsystem and the bosonic density of states completely disappear in accordance with the absence of large octahedra, and the $KBiO_3$ compound should be a Fermi liquid state of a nonsuperconducting metal with a filled valence band of $O2p_\pi$ electrons overlapping with the empty conduction band F with the Fermi level E_F (Fig. 11d). However, due to the presence of a solubility limit of potassium in $BaBiO_3$ ($x \approx 0.5$), the $KBiO_3$ compound exists only hypothetically. Therefore, for the analysis, we use the electron structure of the actually existing nonsuperconducting $BaPbO_3$ metal, which is an electron analogue of the hypothetical compound $KBiO_3$. Because the results of band structure calculations [28] and experiments on photoelectron spectroscopy [58, 59, 71] indicate a shift of the Fermi level in $BaPbO_3$ towards lower energies by 0.25–0.5 eV relative to $BaBiO_3$, we believe that a similar shift should be observed in $KBiO_3$. In our view, this energy shift arises during the transition from the bosonic dielectric $BaBiO_3$ with its own chemical potential μ_0 ($x = 0$) to the nonsuperconducting metal $KBiO_3$ with its own chemical potential μ_F (the Fermi level E_F) ($x = 1$) (see Fig. 11).

It is useful to note that the results of our XFEL experiment provide new arguments to confirm the splitting of Bi 4f lines in superconducting $Ba_{1-x}K_xBiO_3$ compositions, discovered in XPS experiments [25, 72, 73]. These observations, in our opinion, play an essential role in understanding the superconductivity mechanism in bismuthates. As we have already noted, our results show that the ground state of $BaBiO_3$ (Fig. 10a) can be regarded as a two-particle (bosonic) analogue of a conventional semiconductor with a band gap E_b and a bosonic chemical potential μ_0 in the center of this band. This level μ_0 is common to all octahedra, which determines the absence of splitting of Bi 4f states referenced to μ_0, and indicates the same valence state Bi^{3+} of all bismuth ions in $BaBiO_3$ [25, 72, 73]. In superconducting $Ba_{1-x}K_xBiO_3$, local electron hole pairs are preserved in the bosonic subsystem with its chemical potential μ_0. At the same time, at $x \geqslant 0.37$, additional unpaired holes in small octahedra form a conduction band together with valence $O2p_\pi$ electrons in the fermionic subsystem with its own fermionic chemical potential μ_F (the Fermi level E_F). Because the fermionic and bosonic subsystems are spatially separated (i.e., belong to different octahedra) [15, 17], the binding energies of Bi 4f states in large and small octahedra, referenced to two different chemical potentials, are also separated. This leads to broadening of 4f lines [72, 73] and their splitting when observed in photoelectron spectra with high energy resolution at a synchrotron source [25, 74], which indicates the emergence of two valence states of bismuth in superconducting $Ba_{1-x}K_xBiO_3$.

We emphasize once again that, in the absence of resonant laser excitation in the parent $BaBiO_3$ compound, there are no free fermionic charge carriers. Single-particle fermionic excitations can arise in the system only due to the destruction of local pairs that have a large binding energy $E_b \gg k_BT$, and therefore the fermionic contribution to static (zero-frequency) charge transfer is negligible for all temperatures.

We also note that, according to the concepts of the bosonic metallic phase [75–85], the bosonic band effectively plays the role of a conduction band for ordinary (nonsuperconducting) transport of local pairs. Moreover, in [75, 80, 81], it was shown in the framework of the simple Hubbard model with attraction that filled and empty bosonic bands usually have different (electron-like and hole-like) dispersion laws if two-particle physics is pro-

jected onto the single-particle representation used to describe the density of states.

7. Superconductivity mechanism in $Ba_{1-x}K_xBiO_3$ based on model of spatially separated Fermi–Bose mixture

As shown in Section 6, for the hypothetical compound $KBiO_3$ at $x = 1$, all $Bi\underline{L}^0O_6$ octahedra transform into $Bi\underline{L}^2O_6$ octahedra. The bosonic subsystem completely disappears, as does the bosonic density of states: $N_B(E) = 0$. Therefore, $KBiO_3$ corresponds to a nonsuperconducting (normal) Fermi metal described by the standard Fermi liquid theory.

Note that experimental attempts to synthesize $KBiO_3$ at high pressure were made in [86]. Unfortunately, these attempts showed only a partial substitution of K^+ ions with Bi^{3+} ions. As a result, the $K_{1-y}Bi_yBiO_3$ composition was obtained in [86].

We emphasize that such partial (rather than complete) substitution leads to the appearance in the system of a certain number of $Bi\underline{L}^0O_6$ octahedra (besides $Bi\underline{L}^2O_6$) and to the formation of local electron pairs in them. It can therefore be assumed that the composition $K_{1-y}Bi_yBiO_3$ can also be described in terms of a spatially separated Fermi–Bose mixture and can also be superconducting. This assumption is confirmed by the experimental results in [86], where a superconducting transition was observed at the critical temperature $T_c = 10.2$ K.

From our reasoning, it also follows that the compound $BaPbO_3$ should be superconducting if divalent Ba^{2+} ions are partially replaced with trivalent ones (for example, La^{3+}), because such a substitution would form local electron pairs, as in the case of bismuth oxides such as $Ba_{1-x}K_xBiO_3$ and $K_{1-y}Bi_yBiO_3$. Indeed, the new $Ba_{1-x}La_xPbO_3$ compound synthesized at high pressure by Menushenkov et al. [87], demonstrated a superconducting transition at $T_c = 11$ K.

In the preceding sections, we advocated the idea of a spatially separated Fermi–Bose mixture to explain the relation between the local crystal and electron structure and the main transport properties of bismuthates $Ba_{1-x}K_xBiO_3$ in the normal state and in other related compounds.

In this section, we describe the microscopic superconductivity mechanism in $Ba_{1-x}K_xBiO_3$ in the metallic doping range $0.37 < x < 0.5$.

As we already briefly mentioned in Section 2, the existence of a double-well potential of oscillations of oxygen ions connecting different octahedra allows considering superconductivity in $Ba_{1-x}K_xBiO_3$ to be the formation of a macroscopic wave function and a long-range order in a system of compact bosonic pairs.

The long-range order is established as a result of tunneling of local electron pairs from one bosonic cluster to the nearest one through a potential barrier in the form of a fermionic cluster located between two adjacent bosonic ones. Delocalization and percolation of pairs from the left bank of the sample to the right one with sequential repetition of tunneling processes of this type makes it possible to form a coherent state and a macroscopic wave function in the system.

We begin the analysis of superconductivity in $Ba_{1-x}K_xBiO_3$ with an estimate of the matrix element for pair tunneling in the double-well potential shown in Fig. 5b. The matrix element is defined as follows:

$$t_B \propto \omega_0 \exp(-D), \tag{1}$$

where $\omega_0 = 200$ K is the tunneling rate and

$$D = \frac{1}{\hbar}\int_{x_0}^{x_1} |p|\,\mathrm{d}x \approx \frac{d}{\hbar}\sqrt{2MU} \tag{2}$$

is the semiclassical barrier transparency coefficient in the double-well potential.

In (2), the parameters $U = 500$ K and $d \approx 0.07$ Å are the barrier height and width, and M is the oxygen ion mass taken from [10]. We recall the relation between local pair tunneling and oxygen ion tunneling in Fig. 5; as a result, the large mass of oxygen enters the estimate of the barrier transparency coefficient D in (2).

We also note that the tunneling rate ω_0 in (1) already includes all polaronic effects in bismuthates and is therefore relatively small.

For the concentration range $0.37 < x < 0.5$, a local electron pair centered on soft $Bi\underline{L}^0O_6$ complexes effectively tunnels from one bosonic cluster to the nearest one through a fermionic cluster, which serves as a potential barrier and, depending on the doping level x, contains several rigid $Bi\underline{L}^2O_6$ octahedra.

It is natural to assume that the pairs overcome the fermionic cluster step by step. Each step, corresponding to the transition of a pair to a neighboring octahedron, is accompanied by tunneling of an oxygen ion in the double-well potential.

Thus, the tunneling rate ω_0 is the same for each step. We can consider each step an independent event, and therefore the probability of overcoming the fermionic cluster as a whole can be estimated as the product of the probabilities of each step. Then, the resulting matrix element for pair tunneling through a fermionic cluster, which on average contains $\langle N\rangle$ rigid $Bi\underline{L}^2O_6$ octahedra, has the form

$$t_{\mathrm{eff}\,B} \propto \omega_0 \exp\left(-\langle N\rangle D\right), \tag{3}$$

where, in other words, $\langle N\rangle$ is the average number of tunneling acts or hops. Note that $\langle N\rangle$ is in fact proportional to the linear size of the fermionic cluster.

We can estimate $\langle N\rangle$ using the ratio among the concentrations of fermionic, $Bi\underline{L}^2O_6$, and bosonic, $Bi\underline{L}^0O_6$, octahedra, which is the inverse of the ratio $2n_B/n_F = (1-x)/(1+x)$.

As a result, the linear size of the fermionic cluster in three-dimensional bismuthates is

$$\langle N\rangle = \left(\frac{1+x}{1-x}\right)^{1/3}. \tag{4}$$

Expressions (3) and (4) allow obtaining a reasonable estimate of the critical superconductivity temperature. Namely, we can identify the onset of superconductivity with the Bose–Einstein condensation temperature in the bosonic subsystem. The critical BEC temperature is defined as

$$T_c \propto \frac{n_B^{2/3}}{m_{\mathrm{eff}\,B}} \propto t_{\mathrm{eff}\,B}\, a^2 n_B^{2/3}, \tag{5}$$

where we introduce the heavy bosonic effective mass

$$m_{\mathrm{eff}\,B} \propto \frac{1}{t_{\mathrm{eff}\,B}\, a^2}, \tag{6}$$

which corresponds to the sequence of pair tunneling processes.

It should also be borne in mind that the bosonic density n_B in Eqn (12) for T_c satisfies the relation

$$a^3 n_B = \frac{n_B}{n_0} = \frac{1-x}{2}, \tag{7}$$

which is equivalent to $2n_B/n_F = (1-x)/(1+x)$.

Thus, the expression for the critical temperature is

$$T_c \propto t_{\text{eff B}} \left(\frac{1-x}{2}\right)^{2/3}, \tag{8}$$

where the effective matrix element is given by Eqns (3) and (4).

Now, substituting the parameters of the double-well potential obtained by Menushenkov and Klementev [10] into expression (8) gives $T_c \approx 50$ K at the doping level $x = 0.4$, which exceeds the experimentally measured $T_c \approx 30$ K in the $Ba_{0.6}K_{0.4}BiO_3$ compound.

Qualitatively, this difference can be understood as follows: our simple estimates in expressions (3), (4), and (8) do not take rearrangement effects due to the establishment of phase coherence in the system into account; these effects effectively reduce T_c and (somewhat resembling the physics of the electronic polaron effect [88–93] and Anderson's orthogonality catastrophe [94, 95]) reduce the matrix element $t_{\text{eff B}}$, which, upon closer examination, is proportional to the scalar product of the many-body wave functions of the system before and after each tunneling event.

The rearrangement effects are governed by the parameter $\omega_0\tau$, where ω_0 is the pair tunneling rate and τ is the relaxation time of oxygen ion vibrational modes.

In other words, we must compare the tunneling time for pair transfer from one octahedron to a neighboring one and the effective relaxation time of the phonon subsystem due to soft phonon modes. We note that, in the case of bismuthates, longitudinal phonons are the most effective.

Each time, soft phonon modes help to form a new elastic (deformation) configuration before the next tunneling event. Thus, the many-body wave function of the system (including both the bosonic subsystem of electron pairs and the elastic background due to soft phonon modes) can change significantly during the tunneling time, reducing the effective matrix element $t_{\text{eff B}}$ and the critical temperature of the superconducting transition.

8. Comparison with cuprates

Our observation of the LPDW quantum state in bismuthates has much in common with the recent understanding of the mechanism of high-temperature superconductivity in cuprates proposed in [96, 97]. The authors studied how quantum phase coherence develops across the superconductor–metal–insulator transition by observing quantum oscillations of magnetoconductivity $\hbar/2e$ in the anomalous bosonic metallic state in nanostructured $YBa_2Cu_3O_{7-\delta}$ compounds, similar to the Fermi–Bose mixture in the metallic state of the $Ba_{1-x}K_xBiO_3$ superconductor [15, 17].

In view of the great similarity of bismuthate and cuprate HTSCs [39, 98], including strong anharmonicity due to oscillations of oxygen atoms in a double-well potential [99–105], the transition to a synchronized phase in lattice charge dynamics [104, 106], the coexistence of small bosonic and fermionic charge carriers [107], the observation of pre-pairing [65, 67], and the electron structure behavior in time-resolved experiments [55, 56, 108], we hope to extend our model [10, 15–17] to cuprates [102, 109].

While spin fluctuations are generally considered to be the basic mechanism of superconductivity in HTSC cuprates at hole concentrations less than or equal to optimal (see, e.g., [46, 110–112]), the situation appears to be significantly less trivial with doping above optimal.

In this concentration range, and at concentrations close to the quantum critical point (QCP) in particular, the charge channel associated with proximity to a CDW [113] or with collective oscillations of electron density [114], should also play a very significant role.

The nature of the pseudogap state can also be related in this range to pair fluctuations at temperatures above T_c. To some extent, this pseudogap temperature region between T^* and T_c corresponds to a state resembling the bosonic metal state [75–82] in our description of bismuth oxides.

Moreover, even in strongly underdoped cuprates, at a hole concentration much lower than the optimal concentration, the appearance of local pairs of two composite holes (two spin polarons) is possible [75, 115–118].

We note that each of the composite holes (each spin polaron), in accordance with Laughlin's ideas [119, 120] about spin and charge confinement in quasi-two-dimensional HTSC systems formed from a holon and a spinon [121–123] and connected by an antiferromagnetic (AFM) Bulaevskii–Nagaev–Khomskii–Brinkman–Rice string [124, 125], is in a confinement potential.

At high hole concentrations, within the description of HTSC cuprates by the two-dimensional $t-J$ model, a BCS–BEC crossover is possible between local [117, 118] and extended (Cooper) pairing [111, 112] of two holes in the superconducting d-channel.

We emphasize that, in this concentration range, an analogue of the pair density wave (PDW) announced in review [125] can also arise. We also note that the so-called Uemura plot [126], according to which T_c increases linearly with increasing hole concentration similarly to the situation with a two-dimensional Bose gas, is experimental confirmation of the bosonic nature of superconductivity and the formation of local pairs in weakly doped cuprates.

Thus, the formation and subsequent Bose condensation of local pairs are not exclusively a property of ultracold quantum Fermi gases and bismuth oxides, but can apply in a much broader context, extending to certain regions of the phase diagram of HTSC cuprates and even twisted bilayer graphene [127].

At the same time, the nature of local pair formation can be quite different, extending from the change of sign of the scattering length in Feshbach experiments on the BCS–BEC crossover in quantum gases and the appearance of a bound state upon dipole interaction of two AFM strings (two spin polarons) in strongly underdoped cuprates [114–118] to the electrochemical nature of pairing of two holes (two electrons) in BiO_6 clusters in bismuth oxides [10, 13–17, 75–79].

9. Conclusions

The recent results in [13, 14] serve as additional experimental confirmation of our previous proposal [15–17] regarding a new type of conducting state, which is also superconducting at low temperatures and can be described by the properties of a spatially separated Fermi–Bose mixture in $Ba_{1-x}K_xBiO_3$ at doping level $x \geqslant 0.37$.

As noted in Section 6, the concentration $x = 0.37$ serves as a percolation threshold, upon overcoming which an infinite percolation cluster is formed in the fermionic subsystem in real space along [100]-type axes in the perovskite lattice (see Fig. 11), which leads to an insulator–metal phase transition in both fermionic and bosonic subsystems simultaneously. This means that, for $x \geqslant 0.37$ in $Ba_{1-x}K_xBiO_3$, a spatially separated Fermi–Bose mixture of free $O2p_\pi$ electrons (fermions) and local electron pairs on $Bi\underline{L}^0O_6$ octahedra (bosons) was formed.

In the energy space of the fermionic subsystem, the percolation phase transition manifests itself in the overlap at the Fermi level E_F of the empty fermionic band F with the occupied valence band of $O2p_\pi$ electrons, while in the bosonic subsystem, the activation gap closes ($E_a = 0$), and electron pairs acquire the capacity of free motion in space through a continuous fermionic cluster along [100]-type axes (Fig. 11c).

Thus, we conclude that, for $x \geqslant 0.37$, two subsystems are effectively present in the system: fermionic and bosonic; the bosonic band is responsible for superconductivity at low temperatures, and the fermionic band is responsible for the appearance of a Fermi liquid state in the system.

At higher temperatures $T > T_c$, the fermionic contribution $\sigma_F(T)$ to the total conductivity of the normal state of the Fermi–Bose mixture $\sigma(T) = \sigma_B(T) + \sigma_F(T)$ substantially shunts the bosonic contribution $\sigma_B(T)$, which manifests itself as two-particle transport in the Hellman and Hartford experiments [70].

We note that, for $x \geqslant 0.37$, when the activation gap vanishes ($E_a = 0$), a bosonic semiconductor transforms into a bosonic metal [13–17].

Thus, we have a beautiful phase diagram of bismuth oxides with a bosonic insulator (semiconductor) state in the $BaBiO_3$ parent compound and at potassium concentration $0 \leqslant x < 0.37$, followed by a bosonic metal shunted by a fermionic component in the Fermi–Bose mixture in $Ba_{1-x}K_xBiO_3$ at concentrations $x \geqslant 0.37$, and, finally, a standard Fermi metal $KBiO_3$ at $x = 1$.

It is useful to note that the interaction of a bosonic metal and a bosonic semiconductor (insulator) with drops of the superconducting order parameter in a matrix of unpaired states and a percolation phase transition in a system of superconducting drops also occurs in the two-dimensional Hubbard model with attraction in the limit of strong Hubbard interaction and strong local disorder at a low electron density [78, 79, 83].

This model (often called the Hubbard–Anderson model) describes the superconductor–insulator transition in thin films of dirty metal [128–134] and may be important for fabricating superconducting flux qubits in granular Al films [135].

It would also be very interesting to conduct more precise measurements of the electron contribution to the specific heat $C_V(T)$ in $Ba_{1-x}K_xBiO_3$ at temperatures of the order of the critical one, $T \sim T_c$, to separate bosonic and fermionic contributions to the thermodynamics of the normal state at $x \geqslant 0.37$.

Note that, in a very simple approximation, the heat capacity of a three-dimensional ideal Bose gas behaves as $C_B(T) \propto (T/T_c)^{3/2}$ at $T < T_c$. At the same time, $C_B = \text{const}$ for $T \gg T_c$ (under rigorous analysis, according to Tolmachev [136], the heat capacity also has a small intermediate section linearly decreasing with temperature slightly above T_c).

When a weak repulsive interaction is switched on in a Bogoliubov Bose gas, we have a typical heat capacity behavior resembling a λ-point for temperatures $T \sim T_c$.

But in a Fermi–Bose mixture, there is an additional fermionic contribution to the specific heat, which is mainly linear in temperature: $C_F(T) \propto \gamma T$. This contribution can in principle destroy the λ-like behavior of the heat capacity for temperatures $T \sim T_c$. We note that the results of experiments on measuring the specific heat that we currently have mainly demonstrate a smooth behavior of the heat capacity near T_c, because in all these experiments the larger lattice contribution is not separated from the smaller electronic one.

We expect that the results presented in this review will give a new impetus to the development of the model of high-temperature superconductivity in oxides with a perovskite structure.

Acknowledgments

The authors are deeply grateful to Andreas Scherz and all the staff of the SCS beamline of the European Free-Electron Laser EuXFEL, as well as to all participants in the experiment conducted for each contribution to achieving the unique result. The authors are also grateful to A.V. Kuznetsov and A.A. Ivanov for help in preparing the manuscript, useful advice, and discussions. M.Yu.K. is grateful to the Basic Research Program of the National Research University Higher School of Economics (HSE).

References

1. Rice T M, Sneddon L *Phys. Rev. Lett.* **47** 689 (1981)
2. Varma C M *Phys. Rev. Lett.* **61** 2713 (1988)
3. Anderson P W *Phys. Rev. Lett.* **34** 953 (1975)
4. Chernik I A et al. *Pis'ma Zh. Eksp. Teor. Fiz.* **48** 550 (1988); *JETP Lett.* **48** 596 (1988)
5. Miyake K *Prog. Theor. Phys.* **69** 1794 (1983)
6. Khomskii D I *Transition Metal Compounds* (Cambridge: Cambridge Univ. Press, 2014)
7. Menushenkov A P et al. *Physica B* **208–209** 295 (1995)
8. Ignatov A Yu, Menushenkov A P, Chernov V A *Physica C* **271** 32 (1996)
9. Menushenkov A P et al. *JETP Lett.* **67** 1034 (1998); *Pis'ma Zh. Eksp. Teor. Fiz.* **67** 977 (1998)
10. Menushenkov A P, Klementev K V *J. Phys. Condens. Matter* **12** 3767 (2000)
11. Balzarotti A et al. *Solid State Commun.* **49** 887 (1984)
12. Bouwmeester R L, Brinkman A *Rev. Phys.* **6** 100056 (2021)
13. Menushenkov A P *JETP Lett.* **121** 562 (2025); *Pis'ma Zh. Eksp. Teor. Fiz.* **121** 589 (2025)
14. Menushenkov A P et al. *Phys. Rev. Research* **6** 023307 (2024)
15. Menushenkov A P et al. *J. Exp. Theor. Phys.* **93** 615 (2001); *Zh. Eksp. Teor. Fiz.* **120** 700 (2001)
16. Menushenkov A P et al. *Physica B* **312–313** 31 (2002)
17. Menushenkov A P et al. *J. Supercond. Novel Magn.* **29** 701 (2016)
18. Sleight A W, Gillson J L, Bierstedt P E *Solid State Commun.* **17** 27 (1975)
19. Bednorz J G, Müller K A *Z. Phys. B* **64** 189 (1986)
20. Mattheiss L F, Gyorgy E M, Johnson D W (Jr.) *Phys. Rev. B* **37** 3745 (1988)
21. Uchida S, Kitazawa K, Tanaka S *Phase Transit.* **8** 95 (1987)
22. Cox D E, Sleight A W *Solid State Commun.* **19** 969 (1976)
23. Cox D E, Sleight A W *Acta Cryst. B* **35** 1 (1979)
24. Franchini C, Kresse G, Podloucky R *Phys. Rev. Lett.* **102** 256402 (2009)
25. Qvarford M et al. *Phys. Rev. B* **54** 6700 (1996)
26. Plumb N C et al. *Phys. Rev. Lett.* **117** 037002 (2016)
27. Mattheiss L F, Hamann D R *Phys. Rev. B* **26** 2686 (1982)
28. Mattheiss L F, Hamann D R *Phys. Rev. B* **28** 4227 (1983)
29. Khazraie A et al. *Phys. Rev. B* **97** 075103 (2018)

30. Dalpian G M et al. *Phys. Rev. B* **98** 075135 (2018)
31. Jurczek E, Rice T M *Europhys. Lett.* **1** 225 (1986)
32. Sarkar S et al. *Nano Lett.* **21** 8433 (2021)
33. Merz M et al. *Europhys. Lett.* **72** 275 (2005)
34. Menushenkov A P, Protasov E A, Chubunova E V *Fiz. Tverd. Tela* **23** 3703 (1981); *Sov. Phys. Solid State* **23** 2155 (1981)
35. Foyevtsova K et al. *Phys. Rev. B* **91** 121114 (2015)
36. Bharath M et al. *J. Phys. Condens. Matter* **32** 055504 (2020)
37. Mott N *Supercond. Sci. Technol.* **4** S59 (1991)
38. Taraphder A et al. *Phys. Rev. B* **52** 1368 (1995)
39. Taraphder A et al. *Int. J. Mod. Phys. B* **10** 863 (1996)
40. Micnas R, Ranninger J, Robaszkiewicz S *Rev. Mod. Phys.* **62** 113 (1990)
41. Bischofs I B, Kostur V N, Allen P B *Phys. Rev. B* **65** 115112 (2002)
42. Unger P, Fulde P *Phys. Rev. B* **47** 8947 (1993)
43. Anderson P W, in *Frontiers and Borderlines in Many Particle Physics, Proc. of the Enrico Fermi Intern. School of Physics, Varenna, Italy, July 1987* (Intern. School of Physics "Enrico Fermi", Course 104, Eds R A Broglia, J R Schrieffer) (Amsterdam: North-Holland, 1988)
44. Zhang F C, Rice T M *Phys. Rev. B* **37** 3759 (1988)
45. Lin H Q *Phys. Rev. B* **44** 4674 (1991)
46. Kagan M Yu, Rice T M *J. Phys. Condens. Matter* **6** 3771 (1994)
47. Kagan M Yu et al. *Phys. Rev. B* **57** 5995 (1998)
48. Kagan M Yu, Val'kov V V, Woelfle P *Low Temp. Phys.* **37** 834 (2011); *Fiz. Nizk. Temp.* **37** 1046 (2011)
49. Emery V J, Kivelson S A, Lin H Q *Phys. Rev. Lett.* **64** 475 (1990)
50. Pei S et al. *Phys. Rev. B* **41** 4126 (1990)
51. Sugai S *Phys. Rev. B* **35** 3621 (1987)
52. Menushenkov A P, Troyan I A, Eremets M I *JETP Lett.* **77** 521 (2003); *Pis'ma Zh. Eksp. Teor. Fiz.* **77** 620 (2003)
53. Mankowsky R et al. *Struct. Dyn.* **4** 044007 (2017)
54. Mitrano M et al. *Sci. Adv.* **5** eaax3346 (2019)
55. Baykusheva D R et al. *Phys. Rev. X* **12** 011013 (2022) DOI:10.1103/PhysRevX.12.011013
56. Jang H et al. *Sci. Adv.* **8** eabk0832 (2022) DOI:10.1126/sciadv.abk0832
57. Gerasimova N et al. *J. Synchrotron Rad.* **29** 1299 (2022)
58. Kobayashi K et al. *Phys. Rev. B* **59** 15100 (1999)
59. Namatame H et al. *Phys. Rev. B* **48** 16917 (1993)
60. Lukyanov A E et al. *Phys. Rev. Research* **2** 043207 (2020)
61. Tajima S et al. *Phys. Rev. B* **32** 6302 (1985)
62. Tajima S et al. *Phys. Rev. B* **35** 696 (1987)
63. Geballe T H, Moyzhes B Y *Physica C* **341–348** 1821 (2000)
64. Agterberg D F et al. *Annu. Rev. Condens. Matter Phys.* **11** 231 (2020)
65. Božović I, Levy J *Nature Phys.* **16** 712 (2020)
66. Bastiaans K M et al. *Science* **374** 608 (2021); arXiv:2101.08535
67. Cheng G et al. *Nature* **521** 196 (2015)
68. Eagles D M *Phys. Rev.* **186** 456 (1969)
69. Hellman E S et al. *Phys. Rev. B* **44** 9719 (1991)
70. Hellman E S, Hartford E H (Jr.) *Phys. Rev. B* **52** 6822 (1995)
71. Nagoshi M et al. *J. Phys. Condens. Matter* **4** 5769 (1992)
72. Wertheim G K, Remeika J P, Buchanan D N E *Phys. Rev. B* **26** 2120 (1982)
73. Wagener T J et al. *Phys. Rev. B* **40** 4532 (1989)
74. Pudelko W R et al. *Physica B* **591** 412226 (2020)
75. Kagan M Yu *Modern Trends in Superconductivity and Superfluidity* (Dordrecht: Springer, 2013)
76. Kagan M Yu, Bianconi A *Condens. Matter* **4** (2) 51 (2019)
77. Kagan M Yu et al. *JETP Lett.* **117** 755 (2023); *Pis'ma Zh. Eksp. Teor. Fiz.* **117** 754 (2023)
78. Kagan M Yu et al. *Zh. Eksp. Teor. Fiz.* **166** 89 (2024)
79. Kagan M Yu, Mazur E A *J. Exp. Theor. Phys.* **132** 596 (2021); *Zh. Eksp. Teor. Fiz.* **159** 696 (2021)
80. Kagan M Yu et al. *Phys. Rev. B* **57** 5995 (1998)
81. Kagan M Yu et al. *Physica B* **284–288** 447 (2000)
82. Kagan M Yu *JETP Lett.* **103** 728 (2016); *Pis'ma Zh. Eksp. Teor. Fiz.* **103** 822 (2016)
83. Mazur E A, Ikhsanov R Sh, Kagan M Yu *J. Phys. Conf. Ser.* **2036** 012019 (2021)
84. Turlapov A V, Kagan M Yu *J. Phys. Condens. Matter* **29** 383004 (2017)
85. Kagan M Yu, Turlapov A V *Phys. Usp.* **62** 215 (2019); *Usp. Fiz. Nauk* **189** 225 (2019)
86. Khasanova N R et al. *Physica C* **305** 275 (1998)
87. Menushenkov A P et al. *Phys. Solid State* **43** 613 (2001); *Fiz. Tverd. Tela* **43** 591 (2001)
88. Kagan M Yu, Kugel K I, Rakhmanov A L *Phys. Rep.* **916** 1 (2021)
89. Kagan Yu, Prokof'ev N V *Zh. Eksp. Teor. Fiz.* **90** 2176 (1986); *Sov. Phys. JETP* **63** 1276 (1986)
90. Kagan Yu, Prokof'ev N V *Zh. Eksp. Teor. Fiz.* **93** 366 (1987); *Sov. Phys. JETP* **66** 211 (1987)
91. Kagan M Yu, Kugel K I, Rakhmanov A L, arXiv:2109.12684
92. Kagan M Yu, Val'kov V V *J. Exp. Theor. Phys.* **113** 156 (2011); *Zh. Eksp. Teor. Fiz.* **140** 179 (2011)
93. Kagan M Yu, Val'kov V V *J. Supercond. Nov. Magn.* **25** 1379 (2012)
94. Anderson P W *Phys. Rev. Lett.* **18** 1049 (1967)
95. Anderson P W *Phys. Rev.* **164** 352 (1967)
96. Yang C et al. *Science* **366** 1505 (2019)
97. Yang C et al. *Nature* **601** 205 (2022)
98. Sleight A W *Physica C* **514** 152 (2015)
99. Bishop A R, Mihailovic D, de León J M *J. Phys. Condens. Matter* **15** L169 (2003)
100. Menushenkov A P et al. *J. Phys. Conf. Ser.* **190** 012093 (2009)
101. Menushenkov A et al. *Z. Kristallogr.* **225** 487 (2010)
102. Menushenkov A P et al. *J. Surf. Investig.* **7** 407 (2013); *Poverkh. Rentgen., Sinkhrotron. Neitron. Issled.* (5) 10 (2013)
103. Menushenkov A *J. Synchrotron Rad.* **10** 369 (2003)
104. Velasco V et al. *Phys. Rev. B* **105** 174305 (2022)
105. Oh J-Y, Yang D-S, Kang B *Ceram. Int.* **49** 25767 (2023)
106. Velasco V et al. *Condens. Matter* **6** (4) 52 (2021)
107. Müller K A et al. *J. Phys. Condens. Matter* **10** L291 (1998)
108. Kim M et al. *Nature Mater.* **21** 627 (2022)
109. Menushenkov A P et al. *J. Supercond. Nov. Magn.* **27** 925 (2014)
110. Schrieffer J R, Wen X G, Zhang S C *Phys. Rev. B* **39** 11663 (1989)
111. Plakida N M et al. *J. Exp. Theor. Phys.* **97** 331 (2003); *Zh. Eksp. Teor. Fiz.* **124** 367 (2003)
112. Plakida N M et al. *Phys. Rev. B* **55** R11997 (1997)
113. Castellani C, Di Castro C, Grilli M *Phys. Rev. Lett.* **75** 4650 (1995)
114. Silkin V M, Efremov D V, Kagan M Yu *Phys. Scr.* **100** 045943 (2025) DOI:10.1088/1402-4896/adbec5
115. Belinicher V I, Chernyshev A L, Shubin V A *Phys. Rev. B* **56** 3381 (1997)
116. Belinicher V I et al. *Phys. Rev. B* **51** 6076 (1995)
117. Kagan M Yu et al. *Phys. Usp.* **49** 1079 (2006); *Usp. Fiz. Nauk* **176** 1105 (2006)
118. Kagan M Yu *Fizika Makroskopicheskikh Kvantovykh Sistem* (Physics of Macroscopic Quantum Systems) (Moscow: Izd. Dom MEI, 2014) Lecture course. Seminars
119. Laughlin R B *Phys. Rev. Lett.* **60** 2677 (1988)
120. Fetter A L, Hanna C B, Laughlin R B *Phys. Rev. B* **39** 9679 (1989)
121. Anderson P W *Science* **235** 1196 (1987)
122. Lee P A, Nagaosa N *Phys. Rev. B* **46** 5621 (1992)
123. Lee P A et al. *Phys. Rev. B* **57** 6003 (1998)
124. Bulaevskii L N, Nagaev E L, Khomskii D I *Zh. Eksp. Teor. Fiz.* **54** 1562 (1968); *Sov. Phys. JETP* **27** 836 (1968)
125. Brinkman W F, Rice T M *Phys. Rev. B* **2** 1324 (1970)
126. Wu Y-M et al., arXiv:2501.14138
127. Uemura Y J et al. *Phys. Rev. Lett.* **66** 2665 (1991)
128. Cao Y et al. *Nature* **556** 43 (2018); arXiv:1803.02342
129. Haviland D B, Liu Y, Goldman A M *Phys. Rev. Lett.* **62** 2180 (1989)
130. Feigel'man M V et al. *Ann. Physics* **325** 1390 (2010)
131. Skvortsov M A, Feigel'man M V *J. Exp. Theor. Phys.* **117** 487 (2013); *Zh. Eksp. Teor. Fiz.* **144** 560 (2013)
132. Burmistrov I S, Gornyi I V, Mirlin A D *Phys. Rev. Lett.* **108** 017002 (2012)
133. Kuchinskii E Z, Nekrasov I A, Sadovskii M V *Phys. Usp.* **55** 325 (2012); *Usp. Fiz. Nauk* **182** 345 (2012)
134. Goldman A M, Marković N *Phys. Today* **51** (11) 39 (1998)
135. Grünhaupt L et al. *Nature Mater.* **18** 816 (2019)
136. Tolmachev V V *Teoriya Bose-gaza* (Bose Gas Theory) (Moscow: Izd. MGU, 1969)